Purdue University
Purdue e-Pubs

Open Access Dissertations

Theses and Dissertations

Spring 2015

Circular Bessel field statistics and the pursuit of far-subwavelength resolution

Yulu Chen
Purdue University

Follow this and additional works at: https://docs.lib.purdue.edu/open_access_dissertations

Part of the Electromagnetics and Photonics Commons, and the Optics Commons

PURDUE UNIVERSITY
GRADUATE SCHOOL
Thesis/Dissertation Acceptance

This is to certify that the thesis/dissertation prepared

By Yulu Chen

Entitled
Circular Bessel Field Statistics and the Pursuit of Far-Subwavelength Resolution

For the degree of   Doctor of Philosophy

Is approved by the final examining committee:

KEVIN J. WEBB

DAN JIAO

DAVID D. NOLTE

MARK R. BELL

To the best of my knowledge and as understood by the student in the Thesis/Dissertation Agreement, Publication Delay, and Certification/Disclaimer (Graduate School Form 32), this thesis/dissertation adheres to the provisions of Purdue University's "Policy on Integrity in Research" and the use of copyrighted material.

KEVIN J. WEBB

Approved by Major Professor(s): _____

Approved by: Michael R. Melloch   04/23/2015

Head of the Department Graduate Program   Date

CIRCULAR BESSEL FIELD STATISTICS AND

THE PURSUIT OF FAR-SUBWAVELENGTH RESOLUTION

A Dissertation

Submitted to the Faculty

of

Purdue University

by

Yulu Chen

In Partial Fulfillment of the

Requirements for the Degree

of

Doctor of Philosophy

May 2015

Purdue University

West Lafayette, Indiana

To My Family

ACKNOWLEDGMENTS

I am deeply grateful to my advisor Prof. Kevin J. Webb, whose patience, trust, and support made all these possible. His constant passion for deeply understanding new and important knowledge as well as his optimism have inspired me a lot over the past five years. I would also like to express my sincere gratitude to my committee members, Prof. Dan Jiao, Prof. Mark R. Bell, and Prof. David D. Nolte, for dedicating their time and effort and offering keen observations and insightful advice about my research. In addition, I would like to thank Prof. Jiao for her excellent numerical electromagnetics class, which has provided me with a solid background related to numerical simulations. I would like to thank Prof. Trevor Smith of the University of Melbourne for his contributions on the far-subwavelength resolution work. I thank Dr. Huikan Liu, Dr. Vaibhav Gaind, Dr. Shivanand, Dr. Jason Newman, Dr. Hsiao-Rho Tsai, Brian Bentz, Sangsik Kim, Dergan Lin, Qianen Luo, Mengren Man, Yu-Chun Hsueh, Andrew Velzen, Li-Fan Yang, and Bangda Zhou for their comments, contributions, and companion.

I also want to thank my parents, Jie Chen and Ruowei Liu, and my grandparents, Lianyin Yang, Yeqin Chen, Baoshan Liu, and Yuying Yu. Without your unconditional love, care, and support, I would never have become who I am today. Finally, I thank my beautiful girlfriend, Fei Xie, for being with me.

TABLE OF CONTENTS

LIST OF TABLES

LIST OF FIGURES

Figure   Page

ABSTRACT

Chen, Yulu Ph.D., Purdue University, May 2015. Circular Bessel Field Statistics and the Pursuit of Far-Subwavelength Resolution . Major Professor: Kevin J. Webb.

The statistical description of wave propagation in random media is important for many applications. While polarized light in systems with weakly interacting scatterers and sufficient overall scatter has zero-mean circular Gaussian statistics, the underlying assumptions break down in the Anderson localization and weakly scattering regimes. Although probability density functions for wave intensity and amplitude exist beyond Gaussian statistics, suitable statistical descriptions for the field with strong and weak random scatter were unknown. The first analytical probability density function for the field that is effective in both the Anderson localization regime and the weakly scattering regime is derived by modeling the field as a random phasor sum with a random number of contributing terms. This provides a framework for modeling wave propagation in random media, facilitating random media characterization, imaging in and through scatter, and for random laser design.

The resolution of far-field imaging systems is diffraction limited. Super resolution techniques that break the diffraction limit are important in the physical, chemical, and biological sciences, and in technology. An imaging method based on object motion with structured illumination and far-field measurement data that results in far-subwavelength image information is proposed. Simulations show that this approach, with generous detector noise, will lead to the ability to distinguish image features on the nanometer scale with visible light. Along different lines, a perfect negative refractive index can act as a superlens, but realistic materials render this approach ineffective. A method to tune the lens material properties is shown to provide enhanced resolution.

1. INTRODUCTION

1.1   Circular Bessel Statistics and their Applications

The statistical description of electromagnetic fields and intensity can be traced back to the invention of the maser and the discovery of speckle [1, 2]. Speckle forms when coherent waves interact with random media. In general, random media consist of a multitude of randomly positioned objects with a variety of sizes, shapes, velocities, and materials. Examples include cloud, fog, rain, dust, smoke, milk, ground glass, and tissue. Characterization of wave transport (especially laser light in the visible spectrum) in random media plays a pivotal role in imaging and sensing into and through randomly scattering media, which leads to important biological, astronomical, and meteorologic applications.

When light travels through or is reflected from random media, the well-known zero-mean circular Gaussian statistics have been applied to describe field and intensity distributions with great success [3], and have been verified by interferometric measurements in optically thick random scattering media with weakly interacting scatterers [4, 5]. The fundamental assumption of zero-mean circular Gaussian statistics is a random phasor sum model that describes the field as the sum of a multitude of independent random phasors, each representing partial waves traveling through different trajectories inside the random medium or reflected from different parts of a rough surface. Because of the central limit theorem, the probability density function for the real and imaginary parts of the polarized field are Gaussian. Using a simple change of variables, the probability density functions for the intensity and amplitude can be found to be negative exponential and Rayleigh, respectively [3].

The random phasor sum model carries the implicit assumption that the field can be treated as a scalar. In two-dimensional problems, the geometry is translationally

invariant in the third dimension. Because there is no coupling between the two polarizations due to scatter, the solution to 2D problems can be decomposed into transverse electric and transverse magnetic modes. In this case, the out-of-plane component of the field can be modeled by the random phasor sum. For three-dimensional systems, the random phasor sum picture holds for a particular vector field component (co- or cross-pol), as long as there is a sufficiently large number of scattering events so that each orthogonal vector component of the field solution (the scalar) have equivalent statistical information. With weaker overall scatter, however, the temporal response of a random medium has been known to depend on polarization [5], which leads to the development of vector descriptions [6].

Wave transport in random media can be categorized into different regimes, with the scattering mean free path and localization length being two important metrics. The scattering mean free path measures the average distance between successive scattering events, and the localization length is the system size for Anderson localization to occur [7,8]. In the diffusive regime, the scattering mean free path is much larger than the wavelength of the light, but much smaller than the size of the system. This means that the light is scattered multiple times, but the scattered partial waves have little correlation, which is why the Gaussian statistics hold in the diffusive regime. In the weakly scattering regime, there is not enough scatter to completely randomize the incident field. Quantitatively speaking, the system size is then smaller than the transport mean free path, which is a characteristic length over which the memory of the incident field is lost [9]. The scattering mean free path is typically much shorter than the transport mean free path, and is equal to the latter only when the scattering is isotropic [10]. Gaussian statistics do not hold in the weakly scattering regime, because the incident field phasor dominates so that the total field cannot be treated as the summation of a large number of random phasors. In the Anderson localization regime, characterized by the system size being smaller than the localization length, the field forms localized modes, which can be treated as local random cavities formed by random scatterers. Inside these localized modes, the field is the sum of a few

multiply scattered partial waves. Outside the localized modes, there is little field. Consequently, Gaussian statistics do not apply in the Anderson localization regime.

We present a family of circular Bessel probability density functions that are capable of describing the intensity, amplitude, and field statistics of waves in any random medium, with only the assumption of circularity, in Chapter 2 and Chapter 3. Inspired by the K-distribution [11], which treats the field as a random phasor sum with a random number of contributing phasors, we derive the first analytical probability density function for the field that is effective in both the Anderson localization regime and the weakly scattering regime. The field probability density function that we derive and the K-distribution are coherent statistical descriptions that unveil the intrinsic connection between intensity and field, and they are able to model a broader range of statistical phenomena than is possible with zero-mean circular Gaussian statistics. We refer to this family of density functions as "circular Bessel statistics", because both the K-distribution and the field density function that we derive contain Bessel functions. The validity of the circular Bessel statistics has been verified through numerical simulations of electromagnetic waves propagating in 2D random media for both the Anderson localization regime and the weakly scattering regime. Having a set of density functions that work in all scattering regimes provides a framework for modeling wave propagation in random media, facilitating random media characterization, imaging in and through scatter, and random laser design.

1.2 The Pursuit of Far-Subwavelength Resolution

The ability to see tiny things is definitely among one of man's greatest aspirations. It not only satisfies our curiosity, but also has fundamentally important applications in the physical, chemical, and biological sciences. However, the resolution of any imaging system is ultimately limited by the ratio between the wavelength of its source and twice the numerical aperture, $\lambda/(2\text{NA})$, which was found a long time ago [12]. This ratio is frequently referred to as the "diffraction limit". The fundamental reason

for the existence of diffraction limit is the loss of evanescent field information in the far field. Because evanescent fields decay exponentially, they could be easily buried under the noise floor of the detectors, even after a propagation distance of only a few wavelengths.

Researchers have been developing "super-resolution" techniques that can break the diffraction limit for a long time. One simple way to do this is by increasing the numerical aperture by imaging in a medium of large refractive index, such as using an oil immersion microscope [13]. Linear optics nanoscopy based on a random and time varying flow of nanoparticles moving in proximity to the inspected sample has been reported to have nanometer resolution, because the nanoparticles excite the evanescent fields and couple them into harmonic waves [14]. A nonlinear medium mixes modes with high and low spatial frequencies and allows more information to be transferred through the numerical aperture, hence beating the diffraction limit [15]. A holey-structured 3D metamaterial was found to achieve deep-subwavelength acoustic imaging, thanks to the strong coupling between the evanescent field components and the Fabry-Pérot resonances inside the holey structure [16]. Structured illumination using unknown far field speckle patterns can also provide two times improvement of resolution [17]. The fluorescent response of samples, combined with novel illumination schemes [18], gives rise to several remarkable super-resolution microscopy methods, such as stimulated emission depletion (STED) microscopy [19], photoactivated localization microscopy (PALM) [20], and stochastic optical reconstruction microscopy (STORM) [21].

A perfect lens with infinite resolution made of negative refractive index material has been proposed [22]. The inevitable loss in materials and the difficulty of achieving negative permeability at optical frequencies have made the implementation of the perfect lens difficult [23, 24]. With the development of metamaterials, small periodic structures made of metal and dielectric materials (the so-called superlens) have been designed to convert evanescent waves into propagating waves. So far both 1D [25, 26]

and 2D [27] superlenses operating in optical frequency range have been implemented to obtain a three- to seven-fold increase in resolution.

All super-resolution techniques described above have certain limitations. For instance, methods based on fluorescence require labeling of the samples under study, which may be complicated or not feasible for certain samples. In reality, the medium is linear or has very weak nonlinearity in most imaging scenarios, so nonlinearity induced mode mixing may be inefficient [28]. Metamaterial superlenses must be fabricated to a good precision, and placed in the near field in order to couple to evanescent waves. Far field structured illumination cannot obtain resolution improvements better than a factor of two.

We propose an imaging method based on object motion with structured light illumination and far-field measurement data that results in far-subwavelength image information in Chapter 4. Simulations show that this approach, with generous detector noise, will lead to the ability to distinguish image features on the nanometer scale with visible light, without the need for fluorophores.

We find that the transmittance of a negative index slab can be greatly enhanced at a certain spatial frequency if the imaginary parts of the permittivity and permeability in the materials can be tuned, even when all media have overall loss. This leads to a proposed method to image the far-subwavelength features of an object by reconstructing the evanescent part of its spectrum in Chapter 5.

2. CIRCULAR BESSEL STATISTICS AND ANDERSON LOCALIZATION[†]

2.1 Introduction

Zero-mean circular Gaussian statistics are ubiquitously assumed for electromagnetic fields in statistical optics [3]. The validity of this model hinges on the field being made up of a multitude of independent random phasors and weakly interacting scatterers. For example, polarized thermal light has circular complex Gaussian statistics because it contains a large number of independent contributions from each atom in the source. Coherent light can also produce Gaussian statistics after multiple scattering events, as would occur with transmission through certain random scattering media, including, but not limited to, diffusers, particle suspensions, and tissue [1]. Zero-mean circular Gaussian field statistics have been verified experimentally in optically thick random scattering media with weakly interacting scatterers, where the mean free path length, a measure of the mean distance between scattering events, is much larger than the wavelength and long-range correlation effects are negligible [4,5]. In this regime, all of the scattered fields in a random phasor sum description of the field at a point in space can be assumed to be statistically independent.

The statistics of a randomly scattered electromagnetic field can be non-Gaussian, or equivalently, the intensity density function can deviate from negative exponential, when there are a limited number of contributing phasors or when there are correlations between different phasors [29]. The probability density functions for the total transmission and angle-dependent transmission coefficient have been obtained using Feynman diagrams [30,31] and random matrix theory [32]. Instead of studying

[†]This chapter has been published as: Jason A. Newman, Yulu Chen, and Kevin J. Webb, "Zero-mean circular Bessel statistics and Anderson localization," *Phys. Rev. E*, vol. 90, pp. 022119, August 2014

the effects of interference on wave transport, another line of work focused on the properties of the number of contributing random phasors, which led to a family of K-distributions [33, 34]. Such distributions were found to be excellent models for various situations where the intensity statistics are not negative exponential, such as microwave radiation reflected by rough sea surfaces [33], transmission through turbulent atmosphere [35–37], and randomly corrugated waveguides [38].

Despite prior work on the deviation of intensity statistics from negative exponential, an analytical density function has not been achieved that can describe the field statistics when they are not zero-mean circular Gaussian. Inspired by previous work on the K-distribution (modified Bessel function of the second kind) [11, 33, 39], we derive an analytical density function for the real and imaginary parts of the field, assuming only circularity, which is satisfied in media having a sufficiently large number of random scatterers. The resulting circular density function uses a Bessel function description, and is referred to as a circular Bessel density function. The circular Bessel density function contains a degree of freedom that makes it effective in describing the numerical field statistics obtained from strong scatter including the Anderson localization regime [8]. In this paper, we demonstrate that analytic intensity and field density functions based on a circular Bessel function field description are in excellent agreement with numerical data in these strongly scattering regimes.

2.2 Theory

The K-distribution applies to situations where the field is the resultant sum of a randomly varying number of random phasors, N. Its derivation is based on the underlying fluctuation in N, where N is modeled by the negative binomial probability mass function as [11]

$$p(N) = \binom{N + \alpha - 1}{N} \frac{[\langle N \rangle / \alpha]^N}{[1 + \langle N \rangle / \alpha]^{N+\alpha}}. \tag{2.1}$$

The parameter α governs the shape of (2.1). When $\alpha \gg 1$, it is centered around its mean value, $\langle N \rangle$. Thus, for sufficiently large $\langle N \rangle$, any density function derived from

(2.1) will approach Gaussian statistics. When $\alpha \ll 1$, $p(N)$ is peaked at $N = 0$ and then decreases with increasing N, which is the case for localization. This versatility in differing numbers of contributing phasors, N, makes (2.1) applicable to a variety of scattering regimes.

If the contributing random phasors are independent and circular, the characteristic function for the total field amplitude (A), $\psi_A(\omega)$, is the product of the characteristic functions of the amplitudes of the N contributing phasors, $\psi_A(\omega) = J_0^N(a\omega)$, where J_0 is the zeroth order Bessel function of first kind and a is the magnitude of each contributing random phasor [1]. After averaging $\psi_A(\omega)$ over N using (2.1) [11],

$$\langle \psi_A(\omega) \rangle_N = \left(1 + \frac{\omega^2 \langle A^2 \rangle}{4\alpha} \right)^{-\alpha}, \quad \langle N \rangle \to \infty. \tag{2.2}$$

The density function for A is the inverse zeroth-order Hankel transform of (2.2), which in turn leads to the K-distribution for the normalized intensity after a change of variables $(I = A^2)$ and normalization $(\hat{I} = I/\langle I \rangle)$, giving [33, 39]

$$p(\hat{I}) = \frac{2\alpha}{\Gamma(\alpha)} (\alpha \hat{I})^{(\alpha-1)/2} K_{\alpha-1} \left(2\sqrt{\alpha \hat{I}} \right), \tag{2.3}$$

where Γ is the Gamma function, K denotes the modified Bessel function of the second kind, and α is a parameter that is obtained from the variance of $\hat{I}$, such that [39]

$$\sigma_{\hat{I}}^2 = 1 + 2/\alpha. \tag{2.4}$$

We now derive the probability density functions for the field from (2.2). Let ϕ_R and ϕ_I denote the real and imaginary parts of the field, respectively, so the field amplitude is $A = \sqrt{\phi_R^2 + \phi_I^2}$. Assuming that the phase of each random phasor contributing to the total field is uniformly distributed over 2π, the resultant total field will be circular [1]. Then, the characteristic functions for ϕ_R and ϕ_I will be equal to that of the amplitude A [11], given in (2.2), and $p(\phi_R)$ and $p(\phi_I)$ can be obtained by an inverse Fourier transform as

$$p(\phi_{R,I}) = \frac{1}{2\pi} \int_{-\infty}^{\infty} \langle \psi_A(\omega) \rangle_N e^{-i\omega\phi_{R,I}} d\omega \tag{2.5}$$

$$= \frac{2}{\Gamma(\alpha)} \sqrt{\frac{\alpha}{\pi \langle A^2 \rangle}} \left(\sqrt{\frac{\alpha \phi_{R,I}^2}{\langle A^2 \rangle}} \right)^{\alpha-0.5} K_{\alpha-0.5} \left(2\sqrt{\frac{\alpha \phi_{R,I}^2}{\langle A^2 \rangle}} \right). \tag{2.6}$$

We define the normalized real/imaginary part of the field as $\hat{\phi}_{R,I} \equiv \phi_{R,I}/\sqrt{\langle A^2 \rangle}$. Because $\hat{\phi}_{R,I} \equiv \phi_{R,I}/\sqrt{\langle A^2 \rangle}$ is monotonic and invertible, the probability density function for $\hat{\phi}_{R,I}$ can be obtained via a change of variables using (2.6), giving

$$p(\hat{\phi}_{R,I}) = \frac{2}{\sqrt{\pi}\Gamma(\alpha)}\alpha^{(\alpha+0.5)/2}(\hat{\phi}_{R,I}^2)^{(\alpha-0.5)/2}K_{\alpha-0.5}\left(2\sqrt{\alpha\hat{\phi}_{R,I}^2}\right). \qquad (2.7)$$

We call equation (2.7) the circular Bessel density function. It is a counterpart to the well-known zero-mean circular Gaussian density function, and is suitable under circumstances where the central limit theorem does not hold. With this analytical density function for field secured, we proceed to investigate its validity in describing localized fields using numerical simulations.

2.3 Results

The two-dimensional simulation geometry we considered, shown in Fig. 2.1, was an 8 mm long by 2 mm wide region of lithium niobate, LiNbO$_3$ (LN), with randomly distributed 50 μm diameter dielectric-filled holes. The left and right boundaries
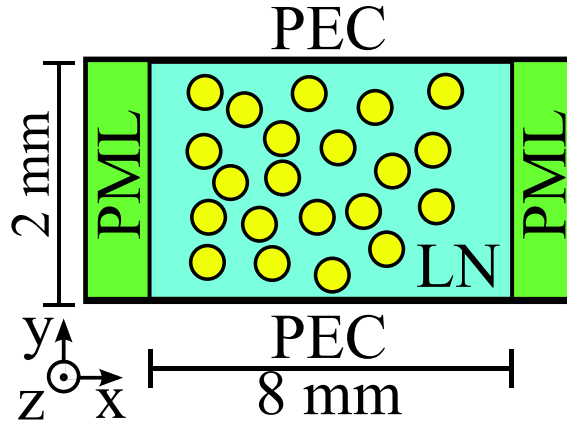
Fig. 2.1. The random medium simulation geometry (not to scale) was composed of randomly distributed 50 μm diameter cylindrical holes in an 8 mm long by 2 mm wide LN region ($\epsilon_r = 41.7$): PML - perfectly matched layer; PEC - perfect electric conductor. A 0.75 THz plane wave with $\mathbf{H}$ in the $\hat{\mathbf{z}}$-direction was incident from the left.

were perfectly matched layers (PML), to absorb the scattered waves, and the top and bottom boundaries were perfect electric conductors (PECs). The boundary on the left was the input plane and that on the right was the output plane. In the simulations, a transverse magnetic 0.75 THz plane wave, an effective wavelength of 62 μm in LN with a dielectric constant of 41.7, with $\mathbf{H}$ in the $\hat{\mathbf{z}}$-direction, was incident from the left (hence, propagating in the $\hat{\mathbf{x}}$-direction), Circular holes were distributed throughout the LN region using a Gaussian density function with a mean x-spacing of $\langle x \rangle$ and a mean y-spacing of $\langle y \rangle$, and variances of σ_x^2 and σ_y^2, respectively. By varying the variance of the Gaussian hole distribution, the holes can be distributed quasi-periodically or highly random, as in the cases presented here. The holes were filled with various dielectrics, with dielectric constants ranging from 1 to 20, where smaller values provide stronger scatter. Due to the large contrast in the dielectric constants of LN and free space, this disordered waveguide geometry has been shown to be an excellent platform to study Anderson localization [40]. Numerical solutions were obtained using finite element method simulations (COMSOL Multiphysics). We investigated two hole distributions, both with a mean fill fraction of 0.42, and mean hole spacings of $\langle x \rangle = 67\mu$m and $\langle y \rangle = 69\mu$m, and $\langle x \rangle = 78\mu$m and $\langle y \rangle = 60\mu$m, corresponding to low and high transmission for the periodic cases, respectively.

We first demonstrate localization of THz waves by analyzing the total transmitted power and intensity statistics at the output plane. The power transmitted through the random medium, T, is the integral of the Poynting vector over the plane of the detector. Let $\hat{T}$ denote the ensemble averaged power transmission, namely $\hat{T} = T/\langle T \rangle$. The characteristic function of $\hat{T}$ was originally derived assuming weak scatter, under general assumptions of flux conservation and time invariance [31, 32]. The probability density function of $\hat{T}$, written as the inverse Laplace transform of its characteristic function, has been shown to be [31]

$$p(\hat{T}) = \int_{-i\infty}^{i\infty} \frac{1}{2\pi i} e^{\xi \hat{T} - g \ln^2 \left(\sqrt{1+\xi/g} + \sqrt{\xi/g} \right)} d\xi, \qquad (2.8)$$

where g is the dimensionless conductance that is related to the variance of $\hat{T}$ by $\sigma_{\hat{T}}^2 = 2/(3g)$ [31,32]. A typical indicator of localization is a dimensionless conductance less than 1 [41,42], a measure of the variance of the transmission statistics. It was later shown experimentally that (2.8) can also be applicable in the localization regime, for both electromagnetic [42–45] and acoustic [46] waves.

(a)   (b)
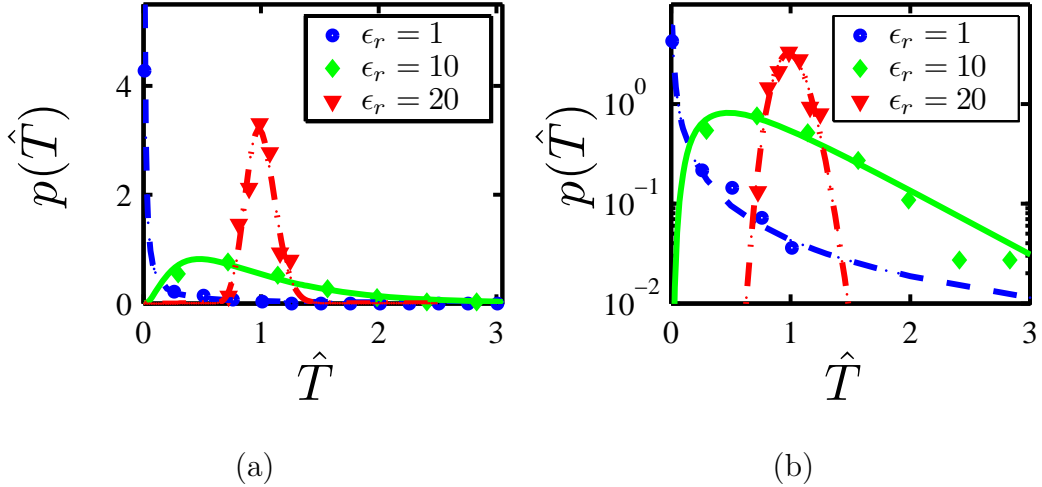
Fig. 2.2. Probability density function of normalized total transmission power, $p(\hat{T})$, from numerical data (symbols) and (2.8) (curves) on linear (a) and semi-log (b) scales. The randomly located 50μm diameter holes in LN ($\epsilon_r = 41.7$) had dielectric constants of 20, 10, and 1, and a fill fraction of 0.42. The hole Gaussian density function had $\langle x \rangle = 67\mu$m, $\langle y \rangle = 69\mu$m and $\sigma_{x,y} = 7\mu$m. As the hole dielectric constant decreases (increasing scatter), g decreases as well.

From our simulation results, we obtained an estimate of g from the variance of $\hat{T}$. We compared $p(\hat{T})$ obtained from our numerical data with (2.8) using the estimated g and then performed a numerical integration. We did this for holes with three distinct dielectric constants (ϵ_r), 1, 10, and 20, with the results shown in Fig. 2.2 [45]. As the dielectric constant increases, it approaches the dielectric constant of the LN background, 41.7, reducing the effective scattering strength. For each dielectric constant, the statistical data was formed from the numerical field data in 90 randomly generated hole distributions. Figure 2.2 shows how $p(\hat{T})$ evolves as g transitions from

42.02 (red) to 1.26 (green) to 0.02 (blue), corresponding to a transition from diffusive transport to localization with increasing strength of scatter. In the diffusive regime there are many "conducting channels" in the random medium, all contributing to the total transmission. Thus, $p(\hat{T})$ is Gaussian as a result of the central limit theorem with weaker scatter (large hole dielectric constant). As localization is approached (with smaller hole dielectric constant), the number of "conducting channels" diminishes, leading to a larger variance in $p(\hat{T})$. These characteristics of $p(\hat{T})$ are all clearly observed in Fig. 2.2. In the case of free space holes ($\epsilon_r = 1$), $g = 0.02$ indicates the localization regime. Note that our numerical results fit the theoretical model of (2.8) well in all three cases, from weak through strong scatter.

We provide a rough estimate of the localization length, $\xi \sim N\ell_s$, where N is the number of propagating modes in our geometry and ℓ_s is the scattering mean free path [42, 47, 48]. We assume that the random medium can be homogenized such that the geometry can be represented as a waveguide filled with a medium with an effective dielectric constant determined by Maxwell-Garnett mixing theory [49, 50]. Thus, the number of modes is equal to $N = 2w/\lambda_e$, where w is the width of the waveguide (2 mm) and λ_e is the effective wavelength in the homogenized medium. For $\epsilon_r = 1, 10,$ and 20, we find that N is equal to 45, 51, and 56 respectively. The scattering mean free path is given by $\ell_s = 1/(\rho\sigma_s)$, where ρ is the density of scatterers and σ_s is the scattering cross section of a single scatterer. After obtaining the scattering cross section from a numerical simulation of the scattered field for a single scatterer, we find the scattering mean free path, ℓ_s, to be 31.7 μm, 39.7 μm, and 91.6 μm for $\epsilon_r = 1, 10,$ and 20, respectively. With both N and ℓ_s calculated, the localization length is be found to be 1.4 mm, 2.0 mm, and 5.1 mm, when ϵ_r is equal to 1, 10, and 20, respectively. The calculation of the dimensionless conductance, the plot of the probability density function of the normalized total transmission, the estimate of the scattering mean free path, and the localization length all serve as important indicators of localization and allow us to establish that LN with randomly placed free space holes can localize THz waves.

We proceed to investigate the intensity probability density function, $p(\hat{I})$, at the output plane, where $\hat{I}$ is the intensity, $\hat{\mathbf{x}}$-component of the Poynting vector, of the magnetic field normalized by its ensemble average. As long as the nth moment of the normalized intensity and total transmission are related by $\langle \hat{I}^n \rangle = n! \langle \hat{T}^n \rangle$ for all positive integers n, $p(\hat{I})$ can be obtained from $p(\hat{T})$ by [31]

$$p(\hat{I}) = \int_0^\infty \frac{1}{\hat{T}} e^{-\hat{I}/\hat{T}} p(\hat{T}) d\hat{T}, \tag{2.9}$$

where $p(\hat{I}|\hat{T}) = \hat{T}^{-1} \exp(-\hat{I}/\hat{T})$ is the conditional density for $\hat{I}$, given $\hat{T}$, arrived at by virtue of the moment dependence between $\hat{I}$ and $\hat{T}$, and Bayes' rule has been used.

(a)	(b)
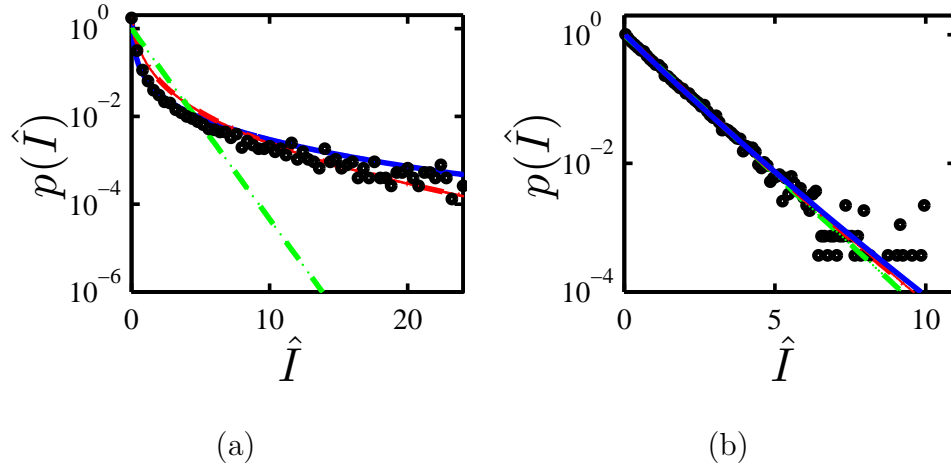
Fig. 2.3. Probability density function for the normalized intensity, $\hat{I}$: negative exponential (green); theoretical result from (2.9) (red); K-distribution (2.3) (blue); numerical data (black dots). The scatterers were 50 μm diameter dielectric holes in LN, where (a) $\epsilon_r = 1$ with $g = 0.32$ and $\alpha = 0.12$, and (b) $\epsilon_r = 20$ with $g = 42$ and $\alpha = 37$. In both figures, the Gaussian-distributed holes had $\langle x \rangle = 78$ μm, $\langle y \rangle = 60$ μm, and $\sigma_{x,y} = 7\mu$m.

We plot numerical $p(\hat{I})$ data at the output plane in Fig. 2.3 for the localization (Fig. 2.3(a)) and diffusive (Fig. 2.3(b)) regimes. Density functions obtained from numerical results are fitted to (2.3) and (2.9). The negative exponential density function is also drawn for comparison.

For the case of strong scatter in Fig. 2.3(a), we observe that both (2.3) and (2.9) fit our numerical data well, while the negative exponential density function decays much faster. This is the first observation that the K-distribution, given by (2.3), can model intensity statistics of Anderson localized waves. In this randomly scattering medium, the number of random phasors that contribute to the total field at a certain position within the random medium is itself random. The number of contributing phasors vanish at positions outside of localization regions, where the field is evanescent, and the number becomes non-zero when the position is within a localization region. These localized regions include concatenated or spatially overlapping localized modes, known as necklace states, that can transmit energy through the random medium [51]. The K-distribution (2.3) fits the data well because (2.1) is an effective model for the number of random phasors that contribute to the field in the strong scatter case. Similarly, in randomly corrugated waveguides having weak scatter and a small number of contributing random phasors, it was found that the output plane field magnitude statistics could be described using the K-distribution [38].

For the case of weak scatter in Fig. 2.3(b), all three models fit the data well, indicating, as expected, a negative exponential probability density function for intensity. Equation (2.3) fits because it approaches a negative exponential density function for $\alpha \gg 1$, while (2.9) fits because $p(\hat{T})$ is Gaussian, with a mean of unity and small variance (approximately a Dirac delta function) in the diffusive regime. Then, $p(\hat{T})$ sifts out $\exp(-\hat{I})$ in (2.9), making the density function for $\hat{I}$ negative exponential.

The distribution for the logarithm of the normalized intensity in the localization regime has been predicted to be log-normal [48, 52, 53]. From (2.3), we can do a change of variables and obtain the K-distribution for $\ln\hat{I}$ as

$$p(\ln\hat{I}) = e^{\ln\hat{i}}\frac{2\alpha}{\Gamma(\alpha)}(\alpha e^{\ln\hat{i}})^{(\alpha-1)/2}K_{\alpha-1}\left(2\sqrt{\alpha e^{\ln\hat{i}}}\right). \tag{2.10}$$

In Fig. 2.4, we plot the numerical distribution of the natural logarithm of the normalized intensity data and compare it with both (2.10) and the Gaussian density function for $\ln\hat{I}$. The log scale provides an expanded view for normalized intensities less than one, which in Fig. 2.3 represents a small portion of the overall plot. The excellent
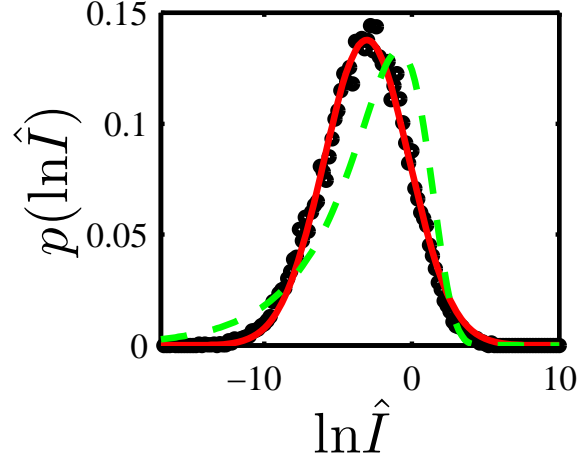
Fig. 2.4. Probability density function for the natural logarithm of normalized intensity, $\ln\hat{I}$: fit to (2.10) with $\alpha = 0.267$ (green dashed); fit to Gaussian with mean $\mu = -3.05$ and variance $\sigma^2 = 8.37$ (red); numerical data (black dots). The numerical data is the same as in Fig. 2.3.

agreement between the data and Gaussian fit provides additional evidence for Anderson localization. On this scale, the K-distribution also fits the data reasonably well. The random phasor sum model leading to the K-distribution for intensity allows the derivation of an analytic form for the field density function which, until now, has not been achieved. The similarity and difference between (2.10) and Gaussian density function can be analyzed by studying the asymptotic forms of the modified Bessel function of second kind, $K_\nu(z)$,

$$K_\nu(z) \sim \frac{1}{2}\Gamma(\nu)\left(\frac{z}{2}\right)^{-\nu}, \quad z \to 0 \tag{2.11}$$

$$K_\nu(z) \sim \sqrt{\frac{\pi}{2z}}e^{-z}, \quad z \to \infty \tag{2.12}$$

Substituting (2.11) and (2.12) into (2.10), we obtain

$$p(\ln\hat{I}) \sim e^{\ln\hat{i}}, \quad \hat{I} \to 0 \tag{2.13}$$

$$p(\ln\hat{I}) \sim e^{-e^{(\ln\hat{i})/2}}, \quad \hat{I} \to \infty \tag{2.14}$$

In (2.13) and (2.14) we only retain the term that dominates the asymptotic behavior of $p(\ln\hat{I})$. We observe from (2.13) that $p(\ln\hat{I})$ grows as $\exp(\ln\hat{I})$ as $\ln\hat{I}$ increases from negative infinity. This growth is slower than the form of any Gaussian density function. When $\ln\hat{I}$ approaches infinity, (2.14) indicates that $p(\ln\hat{I})$ decays as $\exp(-\exp((\ln\hat{I})/2))$, which is faster than any Gaussian decay. Figure 2.4 clearly shows these features.
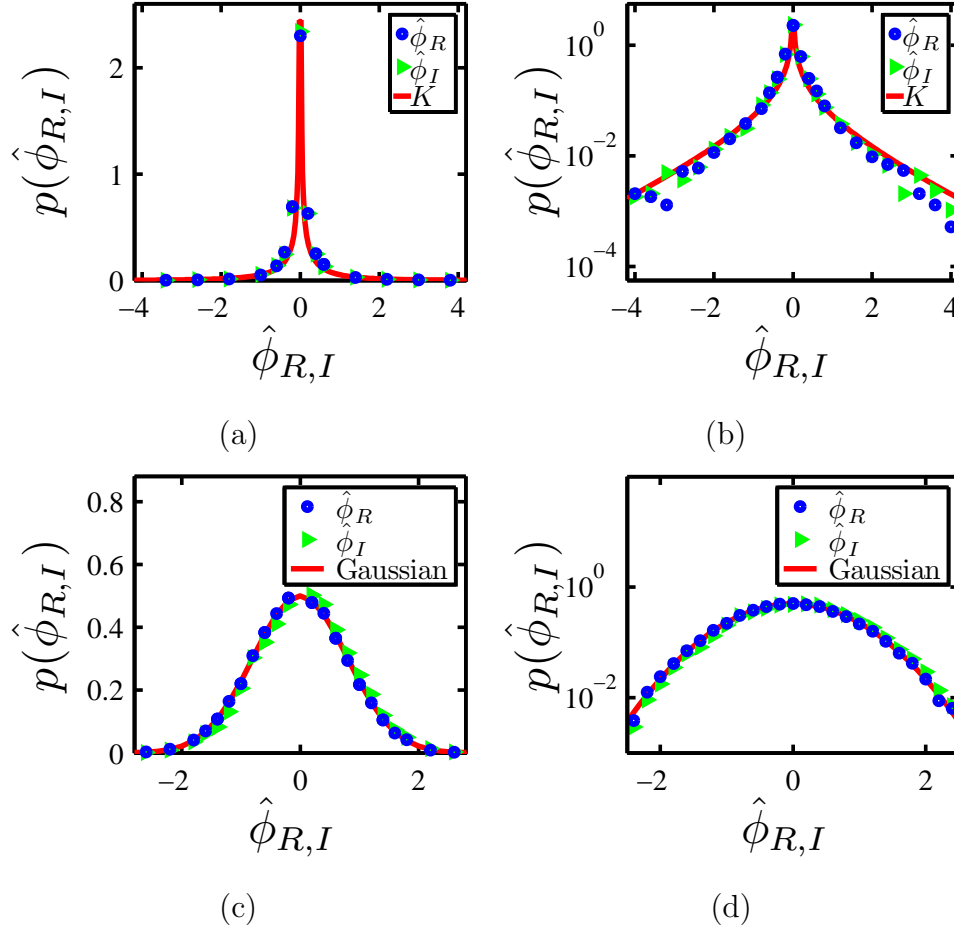
Fig. 2.5. Magnetic field statistics at the output plane, on both linear and semi-log scales for clarity: (a) and (b) are for strong scatter ($\epsilon_r = 1$), where the theoretical line is calculated using (2.7); (c) and (d) show the weak scatter case ($\epsilon_r = 20$), with the red line being the fit to a Gaussian density function. The numerical data is the same as in Fig. 2.3.

Using magnetic field data at the output plane, we obtained the $p(\hat{\phi}_{R,I})$ results in Fig. 2.5, given on both linear and semi-log scales for clarity. Figures 2.5(a) and (b) show the localized case and Figs. 2.5(c) and (d) that for Gaussian fields and weak scatter. We can see that (2.7) is an excellent model for the data, making it the first analytical expression to describe the probability density function of the real and imaginary parts of fields in the localization regime.

Consider now the field statistics inside the random medium for both the diffusive and localization regimes. Referring to Fig. 2.1, numerical field data from the $x = 2$, 4, 6, and 8 mm planes inside the random medium resulted in the probability density functions in Fig. 2.6. We show only the real part of the field for clarity, the imaginary density function is the same. We find identical normalized field statistics at different depths inside the random medium, even in the case of localization.

(a)　　　　　　　　　　　　　(b)
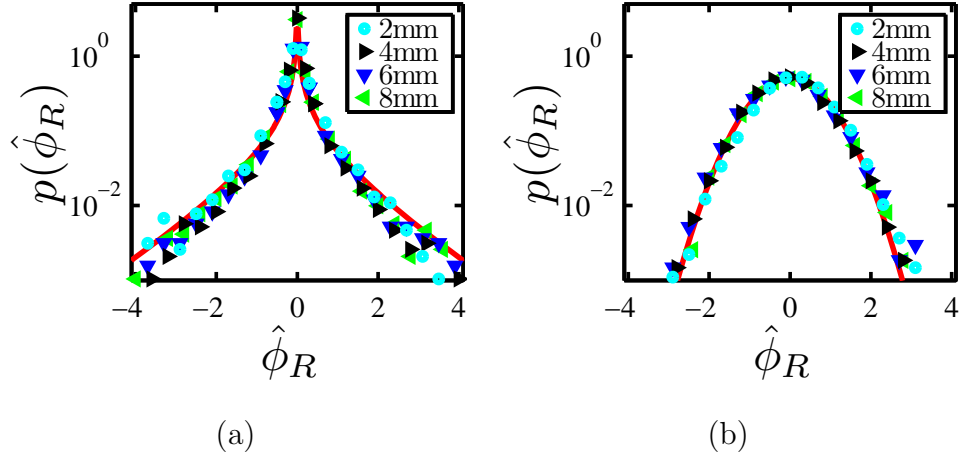
Fig. 2.6. Statistics of the real part of the magnetic field taken at different depths inside the random medium: (a) strong scatter ($\epsilon_r = 1$); (b) weak scatter ($\epsilon_r = 20$). The red line shows the theoretical prediction using (2.7). The numerical field data is the same as that used to generate the results in Fig. 2.3.

The circular Bessel density function, (2.7), has been written in terms of normalized field. However, it has one free variable α that can be traced back to (2.1). It is exactly the different shapes of (2.1) for different α that gives (2.3) and (2.7) their

versatility to model wave statistics under all scattering conditions, with only the minimal assumption of circularity. In Fig. 2.6(a), the invariance of the normalized field statistics as a function of depth is attributed to the contribution of necklace states to the variance (and α) in the localization regime.

All field densities in Fig. 2.6(b) are identical because of the normalization. We know that for zero-mean circular Gaussian statistics, $p(\phi_{R,I}) = \exp(-\phi_{R,I}^2/2\sigma^2)/\sqrt{2\pi\sigma^2}$, and the amplitude is Rayleigh distributed, $p(A = \sqrt{\phi_R^2 + \phi_I^2}) = A \exp(-A^2/(2\sigma^2))/\sigma^2$ [1]. Given that $\langle A \rangle = \sqrt{\sigma^2 \pi/2}$, we can eliminate σ^2 in $p(\phi_{R,I})$ by using $\hat{\phi}_{R,I} = \phi_{R,I}/\langle A \rangle$ as the new random variable, and obtain $p(\hat{\phi}_{R,I}) = 0.5 \exp(-\pi \hat{\phi}_{R,I}^2/4)$. Thus, as long as the fields are zero-mean circular Gaussian, the real and imaginary parts of the field can always be normalized so that they have a probability density function that is independent of position, assuming fully developed statistics. Notice that the peak of the density function in Fig. 2.5(c) is exactly 0.5.

2.4   Conclusion

The fundamental equations of physics, such as Maxwell's equations and the Schrö-dinger equation, use a field or wave function solution that forms the basis for the intensity or probability. Their solutions are typically represented using phasors. Our work contributes to the random phasor sum model by predicting the field density function when the number of contributing random phasors is finite. This holds not only for photon scattering in a variety of random medium, but should also hold for electrons and other particles scattering in random potentials.

We have shown that the numerical field statistics in the localization regime can be well described by the circular Bessel density function. The basis of the circular Bessel density function is the random variation in the number of contributing phasors in the total field, which in turn is tied to the physical picture of Anderson localization. Although the log-normal distribution appears to be a more precise model for intensity in the localization regime, the K-distribution and the circular Bessel density function,

obtained from a modified random phasor sum model, are statistical descriptions that unveil the intrinsic connection between intensity and field, a connection which is not available with the log-normal description. The discovery of the circular Bessel density function for fields builds a theoretical foundation for experiments that directly measure field [40,54]. This density function may also be a basis for the development of a moment theorem analogous to that developed for Gaussian statistics [55], which will facilitate the intensity-based characterization of random media, and imaging through and within random media. The parameter α in the circular Bessel density function is related to the scintillation index (σ_I^2), which has recently been shown to describe a fundamental length scale of waves in random media [56]. Thus, the field density function we derived may also bridge the gap between field statistics and the formation of freak waves in weakly scattering random media. Having an analytical density function that works in a variety of scattering regimes may also prove interesting in the study of random lasers [57], for example, in the design of highly directional random lasers [58].

3. CIRCULAR BESSEL STATISTICS: DERIVATION AND APPLICATION TO WAVE PROPAGATION IN RANDOM MEDIA[†]

3.1 Introduction

In optics, randomness is the rule rather than the exception [1]. Soon after the laser was invented, people noticed that a laser beam reflected from many surfaces displayed high-contrast, fine-scale granular patterns (speckles), which was later attributed to the random roughness of the surfaces [59]. The majority of natural media that light interacts with are random, such as the atmosphere, sea surface, and tissue [60–63]. The random phasor sum model has been used to describe such light-matter interactions, which expresses one polarization component of the field as the sum of multiple random phasors, each conceptually representing light traveling a distinct trajectory [3]. When the number of random phasors becomes very large and the phasors are independent of each other, the central limit theorem holds, resulting in the well-known zero-mean circular Gaussian statistics that give rise to explicit analytical probability density functions for the intensity (negative exponential), amplitude (Rayleigh), and real and imaginary parts of the field (Gaussian) [3].

In a general situation, a random phasor sum picture would be applied to a particular vector field component, leading to a scalar sum description [1]. In three-dimensional systems, scalar theory for a particular vector field component (co- or cross-pol) holds when there are a sufficient number of scattering events so that each orthogonal vector component of the field solution (the scalar) has equivalent information. However, with weaker overall scatter, the temporal response of a random

medium depends on polarization [5], leading to the need to consider vector descriptions [6]. While the response of the co-polarized light is faster with reducing scatter, the scatter needs to be quite weak for the the zero-mean circular Gaussian assumption for this field component to break down [5]. Two-dimensional (2D) problems that are translationally invariant in the third dimension are intrinsically scalar, and can be treated as either transverse electric and transverse magnetic, without coupling between the two polarizations as a result of the scatter. In this case, a scalar model can then be applied to the out-of-plane component of the field.

Zero-mean circular Gaussian statistics break down when the number of contributing phasors is small or significant correlations exist between the phasors. Wave transport in these scenarios has been investigated using the radiative transfer equation (see [7] for a review). Deviations from negative exponential intensity statistics due to mesoscopic correlations have been studied extensively using Feynman diagrams [30,32] and random matrix theory [31]. The resultant density functions have been applied to capture intensity statistics for microwave radiation in random waveguides [45], ultrasound in 3D elastic networks [46], and near-visible light localized in 2D random systems [44].

Despite prior achievements in modeling wave intensity, an analytical density function for field statistics when the central limit theorem does not hold has remained elusive. Maxwell's equations, which are the fundamental equations of electromagnetics, use a field solution that forms the basis for intensity. Thus, studying field statistics can provide insight into various statistical phenomena in electromagnetics at a more fundamental level, such as Anderson localization. In this paper, we provide a detailed derivation of a density function that is capable of describing electromagnetic field statistics in all scattering regimes. Our theory is based on a modified random phasor sum model where the number of phasors that contribute to the field is random. This model has been previously employed to obtain the K-distribution [11,39] — an intensity probability density function that has been used to model microwave intensity reflected by rough sea surfaces [33], transmission through turbulent atmo-

sphere [35–37], and randomly corrugated waveguides [38]. Assuming circularity of contributing random phasors, we obtain the density function for field from a modified random phasor sum model by a simple inverse Fourier transform. The field density function that we derive, together with the K-distribution, describes a broader class of statistical phenomena than is possible with zero-mean circular Gaussian statistics. In Gaussian statistics, the randomness of the number of contributing phasors is not taken into account. We use the term "circular Bessel statistics" because both the K-distribution and the field density function we develop contain Bessel functions. Recently, we introduced the circular Bessel field density function and found it to be an excellent model for field statistics in the Anderson localization regime [64]. Here, we develop and describe in detail the circular Bessel density function and consider applications in both the strong and weakly scattering regimes where Gaussian statistics do not describe the field.

This paper is organized as follows. In Section 3.2, we give a detailed derivation of circular Bessel statistics and discuss its applicability and limitations. A comparison to circular Gaussian statistics is also made. In Section 3.3, we describe numerical simulations performed to verify our density functions and analyze the results. Section 3.4 concludes the paper by summarizing our major findings and discussing potential applications.

3.2   Theory

We derive here the circular Bessel density functions for intensity, amplitude, and the real and imaginary parts of the field. The K-distribution has been previously used for the intensity and amplitude statistics [11, 39]. We extend this work and provide a derivation from first principles, namely the random phasor sum model with a random number of contributing phasors, which covers the intensity, amplitude, and, for the first time, the field statistics. A detailed and self-contained derivation allows us to take full advantage of the circularity assumption of the phasors to obtain the density

functions for the real and imaginary parts of the field, to understand the applicability and limitations of the theory, to establish a meaningful normalization procedure for data analysis, and to give a simple physical interpretation for a variety of statistical phenomena encountered when electromagnetic waves propagate in random media.

3.2.1 Derivation of Circular Bessel Statistics

We assume that the total field, ϕ, can be modeled by the sum of N random phasors,

$$\phi = \sum_{n=1}^{N} \phi_n = \sum_{n=1}^{N} a_n e^{j\theta_n} = A e^{j\theta}. \tag{3.1}$$

We make a few common assumptions regarding the amplitudes and phases of these random phasors [1, 11]: (i) a_n and θ_n are independent of a_m and θ_m for $n \neq m$, (ii) for given n, a_n and θ_n are independent of each other, (iii) all phases θ_n are uniformly distributed over 2π, and (iv) all amplitudes a_n are distributed according to some (unknown) density function $p(a)$.

Consider the characteristic function of the real part of one random phasor [1]

$$\psi_{\phi_{nR}}(\omega) = \int_{-\pi}^{\pi} \int_{0}^{\infty} e^{j\omega a_n \cos\theta_n} p_{a,\theta}(a_n, \theta_n) da_n d\theta_n. \tag{3.2}$$

From assumptions (ii) and (iii), we obtain $p_{a,\theta}(a_n, \theta_n) = p_a(a_n) p_\theta(\theta_n)$ and $p_\theta(\theta_n) = 1/(2\pi)$. Substituting these into (3.2) and integrate with respect to θ_n, we obtain

$$\psi_{\phi_{nR}}(\omega) = \int_{0}^{\infty} \left(\frac{1}{2\pi} \int_{-\pi}^{\pi} e^{j\omega a_n \cos\theta_n} d\theta_n \right) p_a(a_n) da_n = \int_{0}^{\infty} J_0(\omega a_n) p_a(a_n) da_n, \tag{3.3}$$

where J_0 is the zeroth order Bessel function of first kind. The last equality in (3.3) indicates that $\psi_{\phi_{nR}}(\omega)$ is the mean of $J_0(\omega a_n)$ for some random variable a_n. Because all amplitudes a_n are distributed according to some (unknown) density function $p(a)$ (assumption (iv)), we can write (3.3) as

$$\psi_{\phi_{nR}}(\omega) = \langle J_0(\omega a) \rangle_a, \tag{3.4}$$

where $\langle ... \rangle_a$ denotes the average over a. An identical result can be obtained for the characteristic function of the imaginary part, namely

$$\psi_{\phi_{nI}}(\omega) = \langle J_0(\omega a) \rangle_a. \tag{3.5}$$

Because the characteristic function of the sum of several independent random variables is the product of the characteristic functions of the components of the sum, assumption (i) applied to (3.4) and (3.5) leads to the characteristic function of the real and imaginary parts of the total field,

$$\psi_{\phi_R}(\omega) = \psi_{\phi_I}(\omega) = \langle J_0(\omega a) \rangle_a^N. \tag{3.6}$$

In addition, because all random phasors contributing to the field are circular (assumption (iii)), the field should also be circular. This gives an alternative way to write the characteristic function for the real part of the field, leading to

$$\psi_{\phi_R}(\omega) = \int_{-\pi}^{\pi} \int_0^{\infty} e^{j\omega A \cos\theta} p_{A,\theta}(A,\theta) dA d\theta = \langle J_0(\omega A) \rangle_A, \tag{3.7}$$

and the imaginary part of the field has the same characteristic function. Because both (3.6) and (3.7) are the characteristic function of same quantity (ψ_{ϕ_R}), they should be equal. In addition, we can obtain the joint characteristic function of ϕ_R and ϕ_I following the circularity assumption as [1, 11]

$$\psi_{\phi_R,\phi_I}(\omega_R, \omega_I) = \psi_{\phi_R,\phi_I}(\omega = \sqrt{\omega_R^2 + \omega_I^2}) = \langle J_0(\omega a) \rangle_a^N = \langle J_0(\omega A) \rangle_A, \tag{3.8}$$

where ω_R and ω_I are the transform variables for ϕ_R and ϕ_I, respectively.

Now we introduce fluctuations in the number of random phasors, N. Assume that N is a random variable whose probability mass function is the negative binomial distribution [39]

$$p(N) = \binom{N + \alpha - 1}{N} \frac{(\bar{N}/\alpha)^N}{(1 + \bar{N}/\alpha)^{N+\alpha}}, \tag{3.9}$$

where $\bar{N}$ is the mean value of N and α is a positive real parameter. We average (3.8) over N using (3.9), obtaining

$$\langle J_0(\omega A) \rangle_{A,N} = \frac{1}{(1 + \bar{N}/\alpha)^\alpha} \sum_{N=0}^{\infty} \binom{N + \alpha - 1}{N} \left(\frac{\langle J_0(\omega a) \rangle_a \bar{N}/\alpha}{1 + \bar{N}/\alpha} \right)^N, \tag{3.10}$$

where $\langle ... \rangle_N$ denotes the average over the distribution of N. Using the identity [65]

$$\frac{1}{(1-x)^\alpha} = \sum_{N=0}^{\infty} \binom{N+\alpha-1}{N} x^N, \tag{3.11}$$

we finally obtain, from (3.10),

$$\langle J_0(\omega A)\rangle_{A,N} = \left[1 + (1 - \langle J_0(\omega a)\rangle_a)\, \bar{N}/\alpha \right]^{-\alpha}. \tag{3.12}$$

To preserve finite second moments of the field when $\bar{N}$ approaches infinity, we normalize a by $\sqrt{N}$ [1], so (3.12) becomes

$$\langle J_0(\omega A)\rangle_{A,N} = \left[1 + \left(1 - \langle J_0(\omega \frac{a}{\sqrt{N}})\rangle_a \right) \bar{N}/\alpha \right]^{-\alpha}. \tag{3.13}$$

The zeroth order Bessel function of first kind in (3.13), $J_0\left(\omega a/\sqrt{N}\right)$, can be written as the sum of a series of integrals by first considering the Taylor series expansion of the exponential function $\exp\left(j\omega a\cos\theta/\sqrt{N}\right)$, resulting in

$$J_0\left(\omega \frac{a}{\sqrt{N}}\right) = \frac{1}{2\pi}\int_{-\pi}^{\pi}\left(1 + j\frac{\omega a\cos\theta}{\sqrt{N}} - \frac{\omega^2 a^2\cos\theta^2}{2\bar{N}} - j\frac{\omega^3 a^3\cos\theta^3}{6\bar{N}\sqrt{N}} + \cdots \right) d\theta. \tag{3.14}$$

Assuming that $\bar{N} \to \infty$, we retain only the first three terms in the integrand in (3.14) and calculate the integration with respect to θ, which gives

$$J_0\left(\omega \frac{a}{\sqrt{N}}\right) \approx 1 - \frac{\omega^2 a^2}{4\bar{N}}. \tag{3.15}$$

To see that the assumption of large $\bar{N}$ does not necessarily lead to Gaussian statistics, consider the normalized variance of the negative binomial distribution in (3.9) [39]

$$\frac{\sigma_N^2}{\bar{N}^2} = \frac{1}{\bar{N}} + \frac{1}{\alpha}. \tag{3.16}$$

While we have assumed large $\bar{N}$, a small α can still make (3.16) large, skewing the distribution significantly towards small N. An example of the negative binomial distribution is shown in Fig. 3.1 with $\bar{N}$ set to be 100 and two different values of α. In Fig. 3.1 (a), α is equal to 50. The negative binomial distribution is centered around its mean so that the central limit theorem applies, leading to Gaussian statistics. In

Fig. 3.1 (b), we set α to be 0.5 and observe that $p(N)$ is peaked at $N = 0$ and decreases as N grows, which results in the circular Bessel statistics. The ability to incorporate small and random N into the density functions makes the circular Bessel statistics, derived from the assumption of (3.9), applicable to a variety of scattering regimes, which will be discussed further in Section 3.3.

(a)   (b)
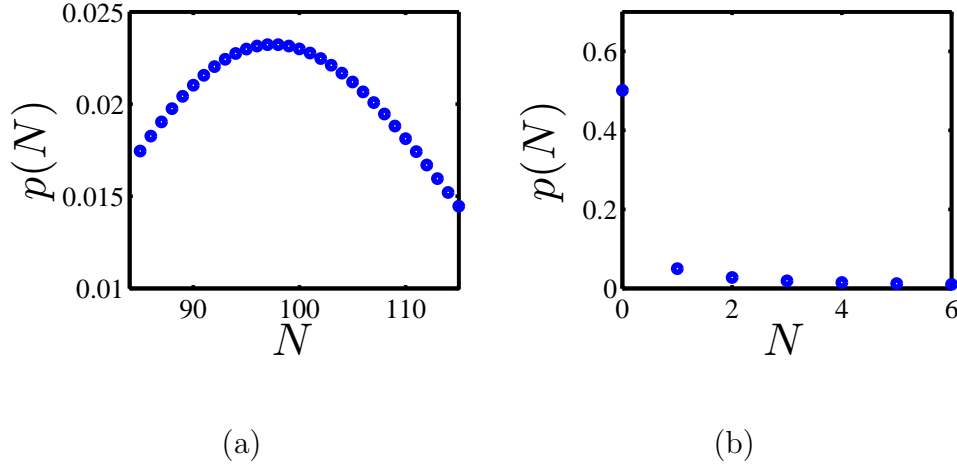
Fig. 3.1. Plot of the negative binomial distribution for (a) $\alpha = 50$, $\bar{N} = 100$, and (b) $\alpha = 0.1$, $\bar{N} = 100$.

A further average of (3.15) over a gives

$$\left\langle J_0\left(\omega\frac{a}{\sqrt{\bar{N}}}\right)\right\rangle_a = \int_0^\infty \left(1 - \frac{\omega^2 a^2}{4\bar{N}}\right) p_a(a)da = 1 - \frac{\omega^2\langle a^2\rangle}{4\bar{N}}. \tag{3.17}$$

Substituting (3.17) into (3.13), we obtain [11]

$$\langle J_0(\omega A)\rangle_{A,N} = \left(1 + \frac{\omega^2\langle a^2\rangle}{4\alpha}\right)^{-\alpha}. \tag{3.18}$$

An inverse Hankel transform of (3.18) secures the radial profile $f(A)$ of the joint probability density function of ϕ_R and ϕ_I as

$$f(A) = \frac{1}{2\pi} \int_0^\infty \left(1 + \frac{\omega^2\langle a^2\rangle}{4\alpha}\right)^{-\alpha} J_0(\omega A)\omega d\omega. \tag{3.19}$$

The probability density function for the field amplitude, A, can be found by multiplying $f(A)$ by $2\pi A$ [1], resulting in

$$p(A) = 2\pi A f(A) = A \int_0^\infty \left(1 + \frac{\omega^2\langle a^2\rangle}{4\alpha}\right)^{-\alpha} J_0(\omega A)\omega d\omega. \tag{3.20}$$

The integration of (3.20) gives the K-distribution for field amplitude A as [11, 33]

$$p(A) = \frac{2b}{\Gamma(\alpha)} \left(\frac{bA}{2}\right)^\alpha K_{\alpha-1}(bA), \qquad (3.21)$$

where Γ is the gamma function and $b = 2\sqrt{\alpha/\langle a^2 \rangle}$. From (3.21), the second moment of A has been calculated to be [39]

$$\langle A^2 \rangle = \frac{4\alpha}{b^2}. \qquad (3.22)$$

From (3.22) and the definition of b, we can see that $\langle A^2 \rangle = \langle a^2 \rangle = \langle I \rangle$.

We define the normalized amplitude $\hat{A}$ as $\hat{A} = A/\sqrt{\langle A^2 \rangle}$. The probability density function for $\hat{A}$ can be obtained from (3.21) by a change of variables as

$$p(\hat{A}) = \frac{dA}{d\hat{A}} p(A) = \frac{4\sqrt{\alpha}}{\Gamma(\alpha)} \left(\sqrt{\alpha}\hat{A}\right)^\alpha K_{\alpha-1}(2\sqrt{\alpha}\hat{A}), \qquad (3.23)$$

upon substituting $b = 2\sqrt{\alpha/\langle A^2 \rangle}$.

Because the mapping between the intensity and the amplitude is monotonic and invertible ($I = A^2$), the probability density function for the intensity can be obtained from (3.21) by a change of variables as

$$p(I) = \frac{dA}{dI} p(A) = \frac{2\alpha}{\langle I \rangle \Gamma(\alpha)} (\alpha I/\langle I \rangle)^{(\alpha-1)/2} K_{\alpha-1}(2\sqrt{\alpha I/\langle I \rangle}). \qquad (3.24)$$

Rewriting (3.24) in terms of the normalized intensity, $\hat{I} = I/\langle I \rangle$, we obtain

$$p(\hat{I}) = \frac{dI}{d\hat{I}} p(I) = \frac{2\alpha}{\Gamma(\alpha)} \left(\alpha\hat{I}\right)^{(\alpha-1)/2} K_{\alpha-1}(2\sqrt{\alpha\hat{I}}). \qquad (3.25)$$

The analytical expressions for all moments of $\hat{I}$ have been obtained [39], and in particular the variance of $\hat{I}$, $\sigma_{\hat{I}}^2 = \langle \hat{I}^2 \rangle - \langle \hat{I} \rangle^2 = \langle \hat{I}^2 \rangle - 1$, has been found to be

$$\sigma_{\hat{I}}^2 = 1 + \frac{2}{\alpha}. \qquad (3.26)$$

This simple relation as been used to estimate the parameter α from numerical data [33].

The probability density functions of the real and imaginary parts of the field can be found by performing an inverse Fourier transform on their respective characteristic functions, given by (3.6) and (3.18). The inverse Fourier transform of (3.18) yields

$$p(\phi_{R,I}) = \frac{1}{2\pi} \int_{-\infty}^{\infty} \left(1 + \frac{\omega^2 \langle A^2 \rangle}{4\alpha}\right)^{-\alpha} e^{-i\omega\phi_{R,I}} d\omega \tag{3.27}$$

$$= \frac{2}{\Gamma(\alpha)} \sqrt{\frac{\alpha}{\pi \langle A^2 \rangle}} \left(\sqrt{\frac{\alpha \phi_{R,I}^2}{\langle A^2 \rangle}}\right)^{\alpha - 1/2} K_{\alpha - 1/2}\left(2\sqrt{\frac{\alpha \phi_{R,I}^2}{\langle A^2 \rangle}}\right). \tag{3.28}$$

We define the normalized real and imaginary part of the field as $\hat{\phi}_{R,I} \equiv \phi_{R,I}/\sqrt{\langle A^2 \rangle}$, whose probability density functions are obtained from (3.28) by a change of variables as

$$p(\hat{\phi}_{R,I}) = \frac{2}{\sqrt{\pi}\Gamma(\alpha)} \alpha^{(\alpha+1/2)/2} \left(\hat{\phi}_{R,I}^2\right)^{(\alpha-1/2)/2} K_{\alpha-1/2}\left(2\sqrt{\alpha\hat{\phi}_{R,I}^2}\right). \tag{3.29}$$

Equation (3.29) is a key result in the sense that it is the first analytical density function that can describe field statistics when the well-known Gaussian density function does not hold. The K-distribution for intensity and the field density function we derived, namely (3.29), are coherent statistical descriptions that unveil the intrinsic connection between intensity and field. We show that (3.29) not only fits field data in the Anderson localization regime very well, it also successfully models residual field statistics in the weakly scattering regime. In addition, (3.29) approaches the Gaussian density function as $\alpha \to \infty$, so it is also effective in the diffusive regime.

3.2.2 Review of Circular Gaussian Statistics

Let $\phi_{R,I}$, A, and I denote the real and imaginary parts of the field, field amplitude, and intensity, respectively. When the field can be regarded as the sum of a large number of random phasors, their density functions are [1]

$$p(\phi_{R,I}) = \frac{1}{\sqrt{2\pi\sigma^2}} e^{-\phi_{R,I}^2/(2\sigma^2)} \tag{3.30}$$

$$p(A) = \frac{A}{\sigma^2} e^{-A^2/(2\sigma^2)} \tag{3.31}$$

$$p(I) = \frac{1}{2\sigma^2}e^{-I/(2\sigma^2)}. \tag{3.32}$$

The mean intensity can be calculated easily from (3.32) to be $2\sigma^2$. Using the same normalization scheme as for the circular Bessel density functions ($\hat{\phi}_{R,I} = \phi_{R,I}/\sqrt{\langle A^2 \rangle}$, $\hat{A} = A/\sqrt{\langle A^2 \rangle}$, and $\hat{I} = I/\langle I \rangle$), we obtain the following probability density functions for normalized field, amplitude, and intensity,

$$p(\hat{\phi}_{R,I}) = \frac{1}{\sqrt{\pi}}e^{-\hat{\phi}_{R,I}^2} \tag{3.33}$$

$$p(\hat{A}) = 2\hat{A}e^{-\hat{A}^2} \tag{3.34}$$

$$p(\hat{I}) = e^{-\hat{I}}. \tag{3.35}$$

Because there are no free parameters in (3.33), (3.34), and (3.35), any difference from the Gaussian statistics can be easily identified when using the normalized density functions to model numerical data.

3.3 Application to Wave Propagation in Random Media

3.3.1 Numerical Simulation

The two-dimensional simulation geometry we considered, shown in Fig. 3.2, consisted of randomly distributed cylindrical scatterers in free space background. The left and right boundaries were perfectly matched layers (PML) to absorb the scattered waves. The top and bottom boundaries were perfect electric conductors (PEC). The left boundary of the free space background was the input plane and the right boundary was the output plane. In the simulations, a transverse electric 0.75 THz plane wave, with $\mathbf{E}$ in the $\hat{\mathbf{z}}$-direction, was incident from the left (hence, propagating in the $\hat{\mathbf{x}}$-direction). Different scatterer materials, together with the size and distribution of the scatterers, allow us to investigate wave transport in a variety of scattering regimes. In each scattering regime, two hundred random realizations of the scatterers were simulated, and numerical solutions were obtained using finite element method (COMSOL Multiphysics).

3.3.2 Results: Anderson Localization Regime

More than half a century ago, Anderson predicted that an electron may not diffuse when placed in a random potential [8]. This phenomenon, Anderson localization, is fundamentally a wave effect with an exponentially decaying spatial wave function given sufficient randomness [66]. The wave nature of this effect has extended the study of Anderson localization beyond electron transport to a broad spectrum of domains [67], including but not limited to acoustics [68] and photonics [69–71]. Photonics offers unique opportunities for research into Anderson localization due to the absence of photon-photon interaction, whereas electrons not only interact with the random potential but also with each other, neglected in the Anderson model [8]. Scaling theory indicates that the waves can always be localized in two-dimensional systems with sufficient size [41]. Localization experiments are typically performed in low-loss and strongly scattering structures, allowing small structure sizes and removal of ambiguities due to absorption [72].

In our 2D simulations, the size of the simulation domain was 8 mm by 2 mm. The scatterers were 80 μm-diameter silicon cylinders ($\epsilon_r = 11.7$), which were distributed
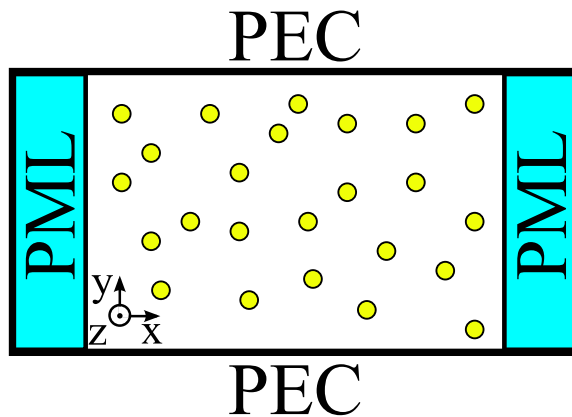
Fig. 3.2. The random medium simulation geometry: PML - perfectly matched layer; PEC - perfect electric conductor. The numerical simulations used a 0.75 THz plane wave with $\mathbf{E}$ in the $\hat{\mathbf{z}}$-direction incident from the left.

throughout the free space background using a Gaussian density function with a mean x-spacing of $\langle x \rangle = 120$ μm and a mean y-spacing of $\langle y \rangle = 120$ μm, and variances of $\sigma_x^2 = 25$ μm and $\sigma_y^2 = 25$ μm, respectively. The significant difference between the relative permittivities of the background and scatterers makes this geometry a good platform to study Anderson localization.

The localization length, ξ, and the scattering mean free path, ℓ_s, are two important length scales that characterize the transport regime. These two quantities are related by $\xi \sim N\ell_s$, where N is the number of open channels (modes) in the randomized waveguide. To obtain the scattering mean free path, $\ell_s = 1/(\rho\sigma_s)$, we calculated the scattering cross section of a single scatterer, σ_s, by numerical simulation of the scattering of a single scatterer in the free space background, and the density of scatterers, ρ, was computed from the scatterer size and distribution. The mean free path was found to be 31.0 μm. As an estimation, we homogenized the randomized waveguide using J. C. M. Garnett mixing theory [49] and found $N = 15$. Hence the localization length is 0.47 mm, significantly shorter than the length of the geometry.

Let $\hat{T}$ denote the power transmission coefficient normalized by its ensemble average, namely $\hat{T} = T/\langle T \rangle$. In the diffusive regime, the variance of $\hat{T}$ has been shown to relate to the dimensionless conductance, g, by $\sigma_{\hat{T}}^2 = 2/(3g)$ [31, 32]. This relation, later used beyond the diffusive regime, provides a simple means to estimate g, which serves as an indicator for Anderson localization ($g < 1$) [42–46]. We obtain from the variance of $\hat{T}$ that $g = 0.81$, which is another signature of Anderson localization.

We plot the statistics of $\phi = E_z$ in the output plane in Fig. 3.3 with the parameter $\alpha = 1.1$ (obtained by (3.26) using numerical data). In Fig. 3.3, we observe an excellent match between the numerical data and the circular Bessel density functions, while the zero-mean circular Gaussian field and negative exponential intensity statistics fail to model the numerical data. This can be explained by the physical picture of Anderson localization, where the number of random phasors (N) that contribute to the total field at a certain position is random. N vanishes in positions outside of localization regions, where the field is evanescent, and becomes non-zero ($N \neq 0$)

Fig. 3.3. Electric field statistics at the output plane in the Anderson localization regime. (a) The probability density functions for normalized intensity, $p(\hat{I})$, are compared with numerical data (black dots): fit to the circular Bessel density function in (3.25) (solid red line); negative exponential density function (3.35) (dashed green line). (b) The probability density functions for normalized amplitude, $p(\hat{A})$, are compared with numerical data (black dots): fit to the circular Bessel density function in (3.23) (solid red line); Rayleigh density function (3.34) (dashed green line). (c) The probability density functions for normalized real/imaginary part of field, $p(\hat{\phi}_{R,I})$, compared with numerical data (blue dots/cyan triangles): fit to the circular Bessel density function in (3.29) (solid red line); Gaussian density function (3.33) (dashed green line). (d) is the field data in (c) shown on log scale for clarity. The numerical data was from 80 μm-diameter silicon cylinders distributed throughout the free space background in the geometry of Fig. 3.2. The positions of the cylinders were obtained using a Gaussian density function with $\langle x \rangle = 120$ μm, $\langle y \rangle = 120$ μm, and $\sigma_{x,y} = 25$ μm.

when the position is within a localization region. The localized regions are usually isolated localized modes due to delicate interference effects between a few multiply scattered partial waves. This can also be understood as a high quality factor cavity formed by multiple randomly positioned scatterers. Because the spatial support of localized modes only spans a small part of the scattering medium, $p(N \neq 0)$ is small, which perfectly matches the negative binomial distribution with small α (Fig. 3.1 (b)).

Occasionally several localized modes can overlap in space and transmit energy efficiently through the random medium, a statistical phenomena known as necklace states [51]. In Fig. 3.4 we show the energy density (normalized with respect to the largest value in space for clarity) and the time-averaged Poynting vector in the $\hat{\mathbf{x}}$-direction for two example realizations of the random scatterer distribution. Although the scatterer positions in these two examples are generated from the same distribution, the field inside the random medium exhibits drastically different behaviors. In Fig. 3.4 (a) and (b), the energy density and the magnitude of Poynting vector are very small 3 mm into the medium, which is typical for localization. In Fig. 3.4 (c) and (d), an instance of necklace states is shown. The high energy density and large magnitude of the Poynting vector that exist throughout the random medium demonstrate that energy is transmitted through effectively. The total transmitted power in Figs. 3.4 (c) and (d) is two orders of magnitude larger than that in Figs. 3.4 (a) and (b).

3.3.3 Results: Diffusive Regime

In optically thick random scattering media with weakly interacting scatterers, the field can be assumed to be the sum of a large number of independent random phasors so that Gaussian statistics hold. The background was assumed to be free space of size 16 mm by 8 mm, where 200 μm-diameter dielectric cylinders ($\epsilon_r = 3$) were distributed throughout using a Gaussian density function with a mean x-spacing of $\langle x \rangle = 1$ mm and a mean y-spacing of $\langle y \rangle = 1$ mm, and variances of $\sigma_x^2 = 200$ μm and $\sigma_y^2 = 200$ μm,
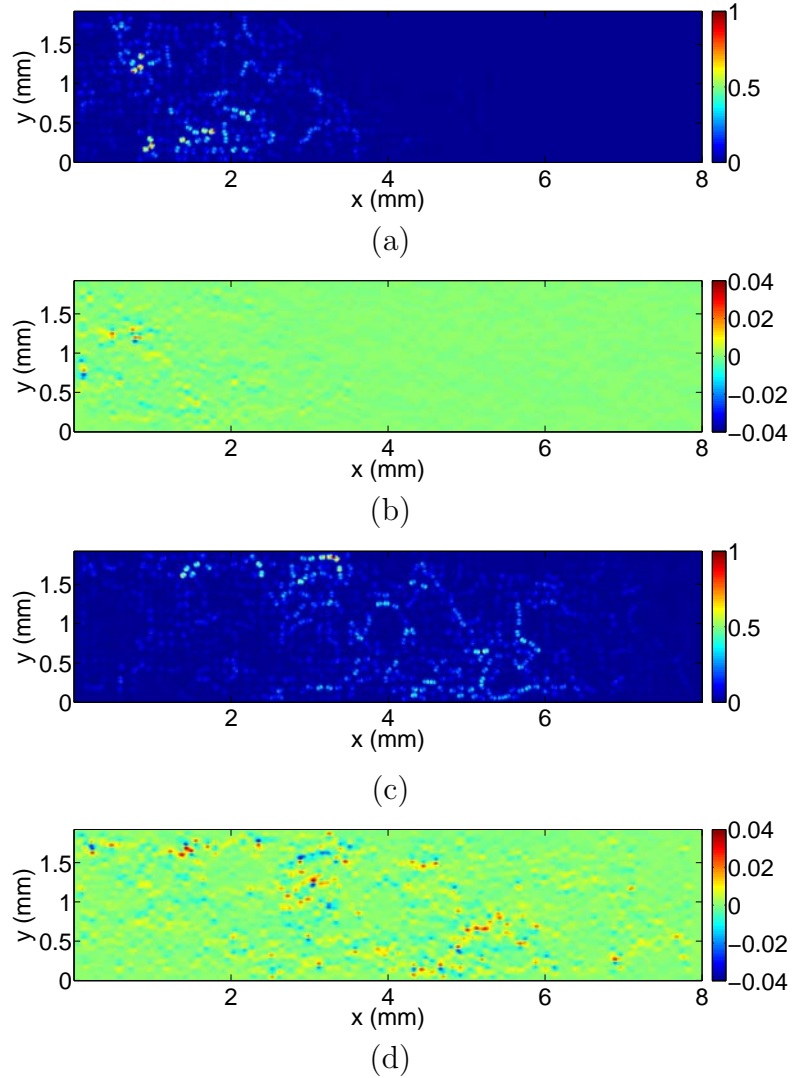
Fig. 3.4. The energy density and the time-averaged Poynting vector in the $\hat{\mathbf{x}}$-direction inside two example random samples are shown. The numerical data was from 80 μm-diameter silicon cylinders distributed throughout the free space background in the geometry of Fig. 3.2. The positions of the cylinders were obtained using a Gaussian density function with $\langle x \rangle = 120 \ \mu$m, $\langle y \rangle = 120 \ \mu$m, and $\sigma_{x,y} = 25 \ \mu$m. (a) and (b) show typical results where the energy density and power flow through the random medium decrease significantly with depth. (c) and (d) show a random sample where there are high energy density and large power flow deep within the sample.

respectively. Using $\sigma_{\hat{T}}^2 = 2/(3g)$, we found the dimensionless conductance, g, to be 21, which indicates diffusive transport [42]. The scattering mean free path and localization length in this case are 3.8 mm and 152 mm, respectively.

In Fig. 3.5, we plot the statistics of $\phi = E_z$ in the output plane with the parameter $\alpha = 43$ (obtained by (3.26) using numerical data). From (3.16), a large α corresponds to a small variance of the negative binomial distribution. Together with the assumption $\bar{N} \to \infty$ in the derivation of circular Bessel statistics, this describes a random phasor sum with a large number of contributing phasors, which holds in the diffusive regime. Both the circular Bessel statistics and the circular Gaussian statistics match the data in Fig. 3.5 extremely well.

3.3.4   Results: Weakly Scattering Regime

We have shown that the circular Bessel density functions can model field statistics in the diffusive regime and the Anderson localization regime. Now we show that they are equally applicable in the crossover from ballistic to diffusive wave propagation, in the weakly scattering regime. By weakly scattering regime, we mean that there is not enough scatter to completely randomize the incident coherent field, so that the incident field phasor dominates the random phasor sum and Gaussian statistics do not hold. A weakly scattering medium can be any system whose length is shorter than one transport mean free path, which is the characteristic length over which the memory of the incident field is lost [9]. The transport mean free path is typically much longer than the scattering mean free path, and is equal to the latter only when the scattering is isotropic [10, 73].

The total field, ϕ, can be regarded as the summation of the incident field and multiple scattered partial waves. In the weakly scattering regime, the amplitudes of scattered fields can be much smaller than that of the incident field, so the total field is not circular. This scenario is shown in Fig. 3.6 (a). The total field can
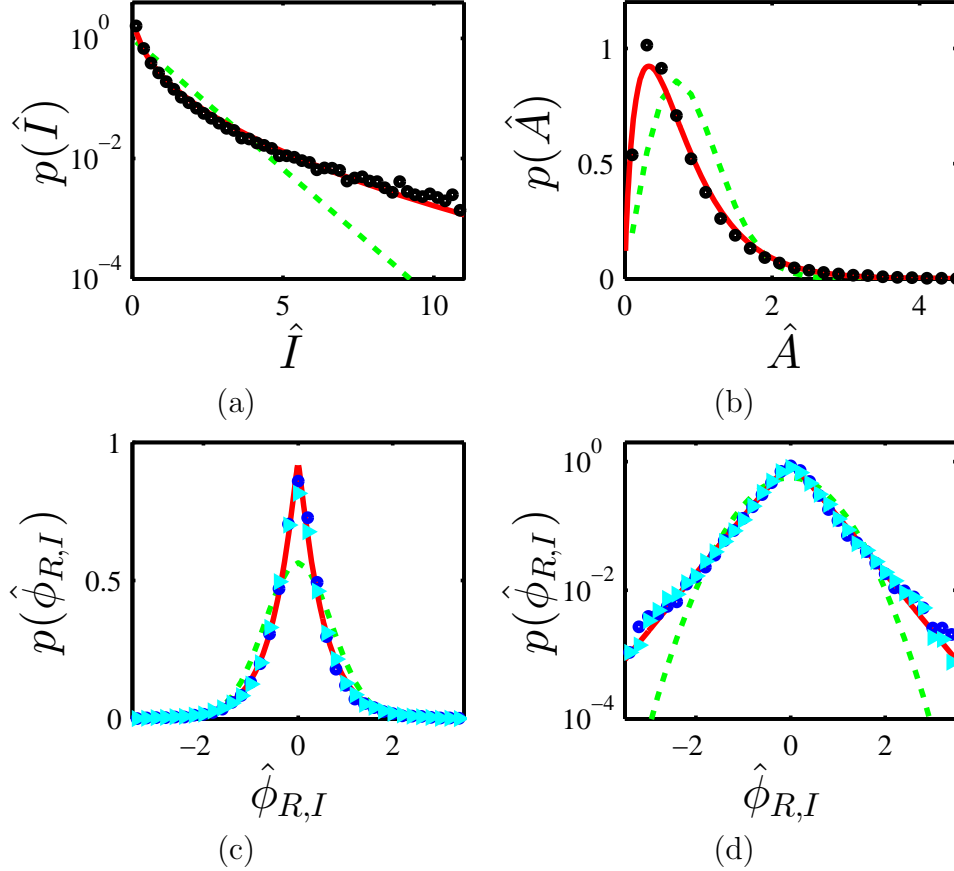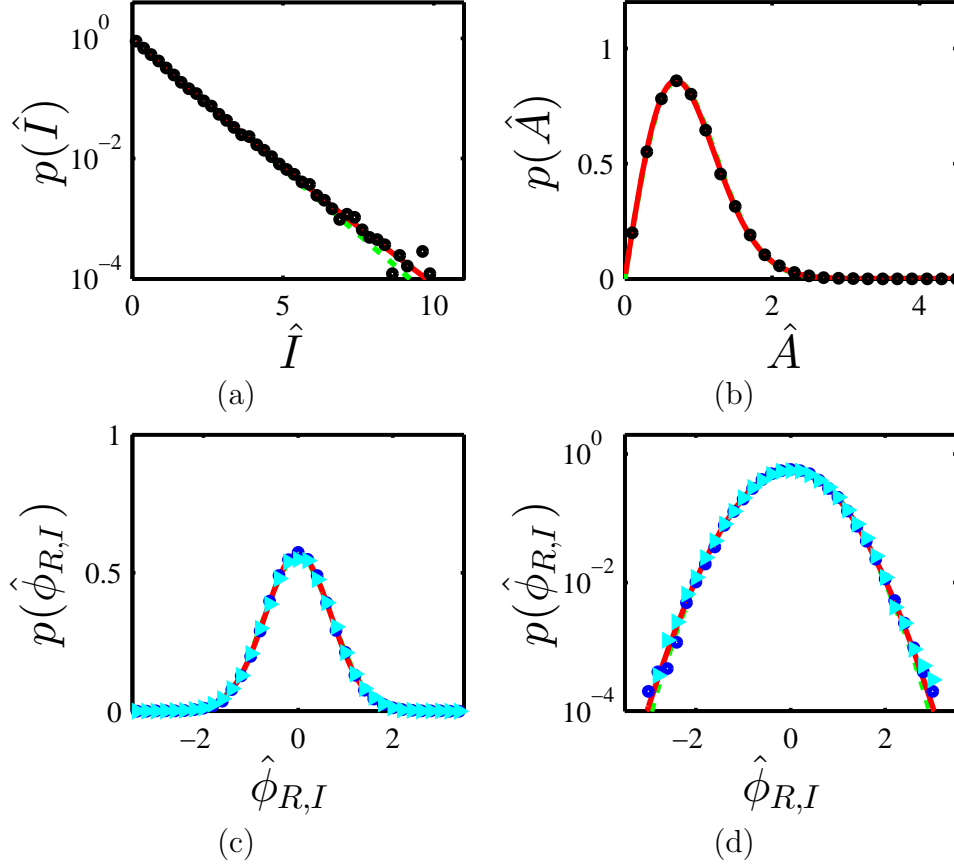
Fig. 3.5. Electric field statistics at the output plane in the diffusive regime. (a) The probability density functions for normalized intensity, $p(\hat{I})$, are compared with numerical data (black dots): fit to the circular Bessel density function in (3.25) (solid red line); negative exponential density function (3.35) (dashed green line). (b) The probability density functions for normalized amplitude, $p(\hat{A})$, are compared with numerical data (black dots): fit to the circular Bessel density function in (3.23) (solid red line); Rayleigh density function (3.34) (dashed green line). (c) The probability density functions for normalized real/imaginary part of field, $p(\hat{\phi}_{R,I})$, compared with numerical data (blue dots/cyan triangles): fit to the circular Bessel density function in (3.29) (solid red line); Gaussian density function (3.33) (dashed green line). (d) is the field data in (c) shown on log scale for clarity. The numerical data was from 200 μm-diameter dielectric cylinders ($\epsilon_r = 3$) distributed throughout the free space background in the geometry of Fig. 3.2. The positions of the cylinders were obtained using a Gaussian density function with $\langle x \rangle = 1$ mm, $\langle y \rangle = 1$ mm, and $\sigma_{x,y} = 200$ μm.
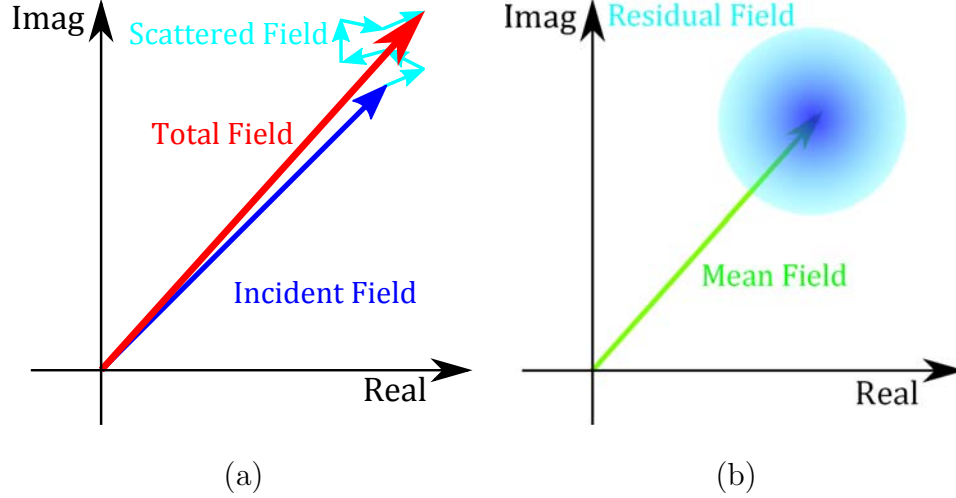
Fig. 3.6. Two ways to model the field: (a) incident field plus scattered field, and (b) mean field plus residual field

alternatively be written as the sum of the mean field (averaged over many random scatterer configurations) and the residual field [74]

$$\phi(\mathbf{r}) = \langle\phi(\mathbf{r})\rangle + \delta\phi(\mathbf{r}), \tag{3.36}$$

shown in Fig. 3.6 (b). The residual field, $\delta\phi$, defined as the difference between the field and its ensemble average in (3.36), has been shown to be circular even in optically thin samples (quasi-ballistic regime) [74].

We simulated THz wave propagation in a 2D random medium consisting of weak scatterers separated by large distances (see Fig. 3.2) and fitted the residual field data to circular Bessel statistics. The background was assumed to be free space of size 6 mm by 4 mm. The scatterers were 200 μm-diameter cylindrical cylinders with $\epsilon_r = 1.5$, distributed throughout using a Gaussian density function with a mean x-spacing of $\langle x \rangle = 1$ mm and a mean y-spacing of $\langle y \rangle = 1$ mm, and variances of $\sigma_x^2 = 400$ μm and $\sigma_y^2 = 400$ μm, respectively. Notice that the relative permittivity of the scatterers is very close to 1, providing weak scatter. The scattering mean free path and localization length in this case are 13.2 mm and 264 mm, respectively. The scattering mean free path is longer than the system length (6 mm), indicating that we are in the weakly scattering regime.
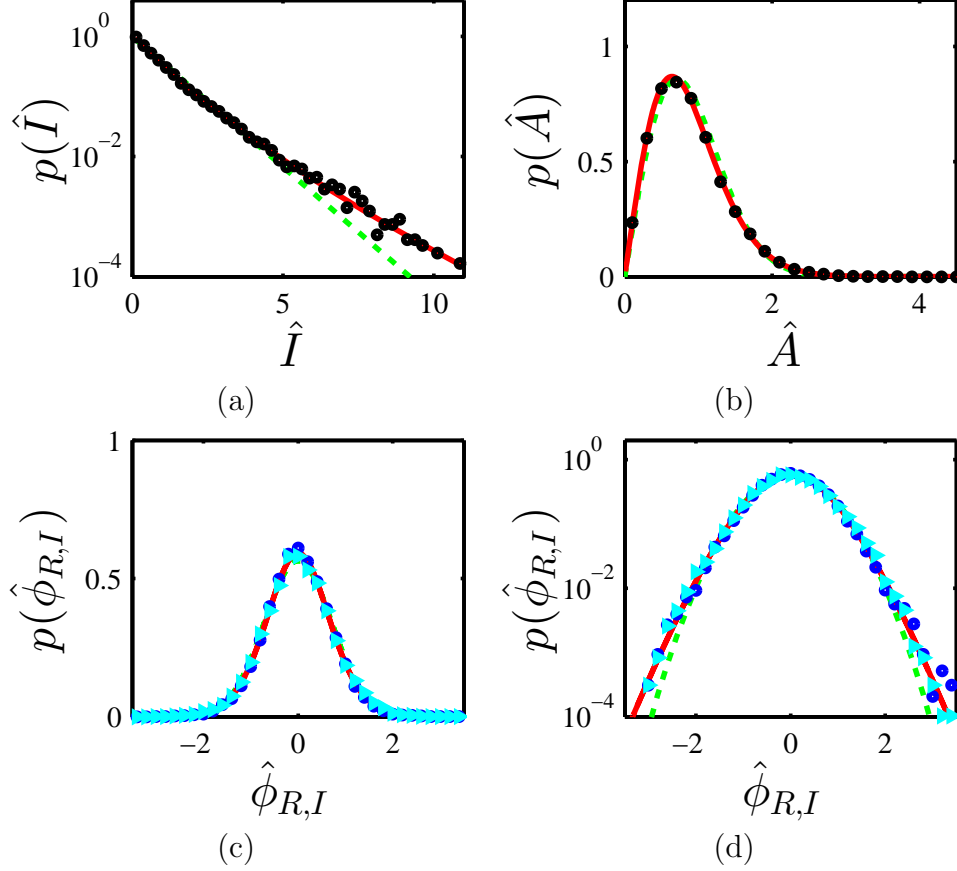
Fig. 3.7. Residual field statistics at the output plane in the weakly scattering regime. (a) The probability density functions for normalized intensity, $p(\hat{I})$, are compared with numerical data (black dots): fit to the circular Bessel density function in (3.25) (solid red line); negative exponential density function (3.35) (dashed green line). (b) The probability density functions for normalized amplitude, $p(\hat{A})$, are compared with numerical data (black dots): fit to the circular Bessel density function in (3.23) (solid red line); Rayleigh density function (3.34) (dashed green line). (c) The probability density functions for normalized real/imaginary part of field, $p(\hat{\phi}_{R,I})$, compared with numerical data (blue dots/cyan triangles): fit to the circular the Bessel density function in (3.29) (solid red line); Gaussian density function (3.33) (dashed green line). (d) is the field data in (c) shown on log scale for clarity. The numerical data was from 200 μm-diameter dielectric cylinders ($\epsilon_r = 1.5$) distributed throughout the free space background in the geometry of Fig. 3.2. The positions of the cylinders were obtained using a Gaussian density function with $\langle x \rangle = 1$ mm, $\langle y \rangle = 1$ mm, and $\sigma_{x,y} = 400$ μm.

In Fig. 3.7, we plot the statistics of the residual field, $\phi = \delta E_z = E_z - \langle E_z \rangle$, in the output plane with the parameter $\alpha = 8.0$ (obtained by (3.26)). We can see that the deviations of the numerical data from Gaussian statistics are beautifully captured by the circular Bessel density functions, such as in Fig. 3.7 (a) for large $\hat{I}$, and in Fig. 3.7(d) for large $|\hat{\phi}_{R,I}|$.

In our simulation, the scatterers are far apart and have a relative permittivity close to the surrounding medium. In this case single scattering is predominant and the Born approximation holds. So the total field at a point in space can be treated as the incident field plus fields scattered by different scatterers. If we return to the random phasor sum model, the number of terms in the random phasor sum should be one (incident field phasor) plus the total number of scatterers in the geometry (scattered field phasors). However, the scattered field decays as $1/\sqrt{\rho}$, where ρ is the distance between the observation point and the scattering center. So the number of scattered field phasors that actually contribute to the total field is small, which is equal to the number of scatterers that lie within a few wavelengths' distance from our point of interest. Because the scatterer positions are random, the number of contributing phasors in space is, of course, random. This explains why the circular Bessel density functions work better than circular Gaussian density functions for modeling the residual field statistics. The previous success of using (3.21) to model field amplitude statistics in randomly corrugated waveguides [38] can be explained by the same argument.

3.3.5 Discussion

We have derived a scalar statistical description (circular Bessel density function) for the field and applied it to a 2D scattering system — the structure and the fields are independent of the $\hat{z}$ coordinate in Fig. 3.2. Considering a 2D system reduces the computational cost in the numerical simulations and the structure is compatible with some experiments that directly measure field [54]. As a further step, it would be inter-

esting to apply the circular Bessel density function to a polarized field measurement in three-dimensional random media. In such scenarios, we expect that the circular Bessel density function should describe a single polarized component of the field as long as there are a sufficient number of scattering events. In the weakly scattering regime, the evolution of co- and cross-polarized light and the application of circular Bessel statistics requires further study.

Both the Gaussian and Bessel density functions are based on the concept of a random phasor sum, which corresponds to the mathematical picture of a total field at a point in space described as the sum of the incident field and scattered fields from different scattering trajectories, each represented as a phasor. Gaussian statistics hold as a result of the central limit theorem, which corresponds to a large number of independent contributing phasors to the field. The circular Bessel density functions, however, assume that the number of contributing phasors is random and can be modeled by the negative binomial distribution (3.9). The choice of negative binomial distribution strikes the balance between analytical tractability and modeling flexibility. While it is necessary to assume $\bar{N} \to \infty$ to retain only the first three terms in (3.14) and obtain analytical density functions, N can still be small and random because the distribution is skewed significantly towards small N when α is small. The case of small and random N corresponds to total field statistics in the localization regime and residual field statistics in the weakly scattering regime. Although it is hardly feasible to determine the exact value of N in large random media, the circular Bessel density functions do provide a means to estimate the distribution of the number of random phasors through the fit of α to measured data and hence gain valuable information on the nature of wave transport inside the random media. If the field is circular, the value of α is a quantitative indicator of the diffusive and localization regimes, where a smaller (larger) α means the transport is more localized (diffusive). If the field is not circular, as is the case in the weakly scattering regime, a smaller α may indicate more ballistic transport. A limiting case is a homogeneous medium where no residual field exists, so $p(N = 0) = 1$ in the random phasor sum model

for residual field. This corresponds to an infinite normalized variance of the negative binomial distribution and $\alpha = 0$, as seen in (3.16).

3.4   Conclusion

We have presented a detailed derivation of the circular Bessel statistics under the modified random phasor sum model where the number of contributing phasors is random. The density functions obtained are found to be excellent statistical descriptions for the intensity, amplitude, and real and imaginary part of electromagnetic waves in a variety of scattering regimes. When the total field is circular, such as in the diffusive and localization regimes, circular Bessel statistics can be directly applied to the total field. When the total field is not circular, due to very weak scatter, it can be used to model residual field statistics. The Schrödinger equation, like Maxwell's equations, also has solutions that can be represented by phasors. Thus, the circular Bessel statistics should also hold for electrons and other particles scattered in random potentials. Because the circular Bessel statistics asymptotically approach the well known Gaussian statistics when $\alpha \to \infty$, it can be regarded not only as a generalization of the latter but also as the foundation of a broader class of statistical phenomena. Theoretically, it is vital in the understanding of the formation of freak waves [56], and can potentially motivate the development of a moment theorem analogous to that developed for Gaussian statistics [55]. Experimentally, it can provide the theory for experiments that directly measure field [54], facilitate random media characterization when designing highly directional random lasers [57,58] and compact spectrometers [75], as well as imaging within and through randomly scattering media.

4. OBJECT MOTION WITH STRUCTURED ILLUMINATION AS A BASIS FOR FAR-SUBWAVELENGTH RESOLUTION[†]

4.1 Introduction

For a very long time it has been accepted that the resolution of any far-field imaging system is fundamentally limited by the wavelength of the radiation and the refractive index of the optics used. For a large numerical aperture lens, this results in a resolution proportional to $\lambda_0/(2n)$, where λ_0 is the free space wavelength and n is the refractive index. The restriction of the maximum achievable resolution to about one half of a wavelength, known as the diffraction limit [12], has driven the use of shorter wavelengths for lithography and optical memory, as well as optics of larger background refractive index (immersion optics) in order to obtain improved resolution. In the case of microscopy, there are various application domains where a dramatically reduced wavelength may not be possible, and there are challenges in manipulating light having a very small wavelength.

The mathematical picture for the diffraction limit comes from a plane wave field expansion in the near-field and the removal of the evanescent fields, which are below the noise floor of a detector in the far-field where most optical systems operate. Use of near-field scanning methods allow measurement of the evanescent fields, but such approaches may not be practical in applications. Structured illumination and the Moiré effect provide a means to determine object information in the far-field with an improvement in resolution of up to a factor of two [76, 77]. Also, phase contrast

[†]This chapter has been submitted for publication as: Kevin J. Webb, Yulu Chen, and Trevor A. Smith, "Object motion with structured illumination as a basis for far-subwavelength resolution."

from an interferometer measurement provides accurate axial (thickness) information, given the refractive index, subject to source and detector noise [78].

Subwavelength spatial resolution has been achieved using fluorescence microscopy [19, 20, 79]. In stimulated emission depletion (STED) microscopy, a patterned beam (such as a donut shape) is scanned along with the excitation beam, and all photoexcited fluorophores are driven to a dark state except those near the center of the point spread function. The spatial resolution is thus defined by the depleting beam, and a lateral resolution of $\lambda_0/45$ and a longitudinal resolution of about three times this have been shown [79]. This approach was limited by the need for reversible photophysical behavior of the fluorophore. In photoactivated localization microscopy (PALM) [20], and in stochastic optical reconstruction microscopy (STORM) [21], a subset of molecules are activated, and it is assumed that the distance between any two of them is greater than $\lambda_0/(2n)$ away. The emitter can then be localized to a precision limited by the determination of the emission peak in space at the detector. While used with great success, these forms of microscopy are limited by the need to introduce (sometimes specific) fluorescent molecules or nanoparticles, a situation that may not always be possible in practice.

We present a new approach for retrieving subwavelength object information that requires neither the introduction of a fluorophore nor the assumption of spatially disparate elements - separated by more than $\lambda_0/(2n)$. By employing a structured incident field and then performing a set of far-field measurements using detector arrays as a function of scanned object position, we show using simulated noisy data that $\lambda_0/100$ resolution can easily be achieved with substantial detector noise. Unlike near-field scanning methods that access small collection volumes and are restricted to surface information, by scanning the object position (a cell, for example), scattered light from the whole object is measured at each of the object positions.
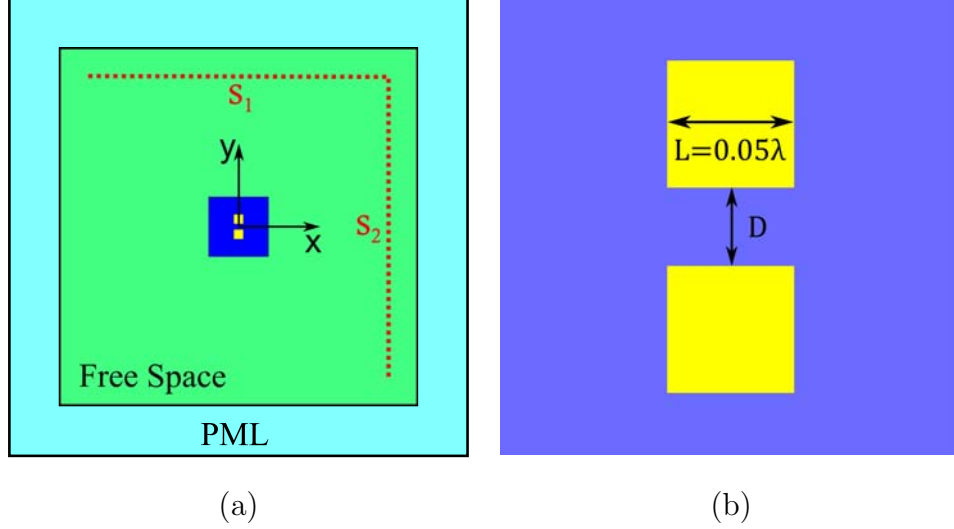
Fig. 4.1. (a) The square 6λ simulation geometry consists of two square scatterers ($\epsilon_r = 1.5$) scanned in 0.1λ steps in 2D. The range of motion is represented by the blue square ($1\lambda \times 1\lambda$) at the center of the free space background. The red dotted lines denote the locations of the detectors. (b) The central scanned region is drawn to explicitly show the dimension and arrangement of the scatterers.

4.2 Numerical Simulation

We consider a 2D simulation geometry where two small square scatterers ($\epsilon_r = 1.5$) are moved around in a free space background, as shown in Fig. 4.1(a). The numerical finite element method (FEM - COMSOL) simulation used an incident field wavelength of $\lambda = 1$ μm, but the problem is scalable, and all data as a function of spatial coordinates are presented in terms of wavelength. The size of the free space background is 6λ by 6λ, and it is surrounded by 2λ-thick perfectly matched layers (PML) on all sides. The square scatterers are of dimension 0.05λ, and their edge-to-edge separation is denoted by D, as shown in Fig. 4.1(b). The two scatterers with fixed relative positions are scanned in both the $\hat{\mathbf{x}}$- and $\hat{\mathbf{y}}$-directions with a step size of 0.1λ over a region of λ by λ (denoted by the blue square in the center of Fig. 4.1(a)).

We use two illumination schemes. The first (PW) is a single plane wave with $\mathbf{E}$ in the $\hat{\mathbf{z}}$-direction and incident from the left, hence propagating in the $\hat{\mathbf{x}}$-direction (assuming $\exp{(j\omega t)}$ dependence) as

$$\mathbf{E} = \sqrt{2}e^{-jkx}\hat{\mathbf{z}}, \tag{4.1}$$

where $k = 2\pi/\lambda$. The second scheme (SI) is the superposition of two plane waves, both having $\mathbf{E}$ in the $\hat{\mathbf{z}}$-direction, one propagating in the $\hat{\mathbf{x}}$-direction and the other in the $\hat{\mathbf{y}}$-direction, giving

$$\mathbf{E} = (e^{-jkx} + e^{-jky})\hat{\mathbf{z}}. \tag{4.2}$$

Two detector arrays, s_1 and s_2, are used to measure power in the transmission direction and are shown as the red dotted lines in Fig. 4.1(a). Both s_1 and s_2 are 0.5 λ from the boundaries, and the length of each is 5 λ.

For the PW case, we use s_2 to measure the time-averaged Poynting vector in the $\hat{\mathbf{x}}$-direction, S_x. For a single plane wave described by (4.1), $S_x = 1/\eta$, where η is the (free space) wave impedance. The total power detected by s_2 is $P_{\mathrm{PW}} = 5\lambda/\eta$. For the SI case, s_1 is also used to measure the time-averaged Poynting vector in the $\hat{\mathbf{y}}$-direction, S_y. From (4.2), $S_x = S_y = [1 + \cos{(kx - ky)}]/(2\eta)$. Therefore, the total power into s_1 and s_2 is $P_{\mathrm{SI}} = 5\lambda/\eta$, identical to the PW case when there is no object present. Equal detected powers for both cases provides a basis for comparison.

Because we are interested in the far-subwavelength distance between the two subwavelength scatterers, we comment on the accuracy of the numerical model before proceeding further. In the FEM simulations, the maximum mesh size was 0.02λ and the minimum mesh size was 0.001λ. There were at least 8 layers of mesh elements between the two scatterers. When the maximum mesh was reduced to 0.01λ, the change in the Poynting vectors was 6 orders of magnitude smaller. We therefore assume that the numerical field solution is sufficient for our purpose.

4.3   Noise Analysis

A key step in establishing spatial resolution is the incorporation of detector noise information. The detector signal-to-noise ratio is $\mathrm{SNR} = \langle i \rangle^2/\sigma_i^2$, where $\langle i \rangle$ is the

average photodetector current and σ_i^2 is the variance. We assume that at each detector the additive (current) noise is a zero-mean Gaussian random variable whose standard deviation is proportional to the detected time-averaged Poynting vector. The noise equivalent power (NEP W/$\sqrt{\text{Hz}}$) is defined as the optical signal power needed to make the electrical SNR=1 in a $B = 1$ Hz bandwidth. Writing $\sigma_i^2 = 2e\langle i_n \rangle B$ for detector integration time $T = (2B)^{-1}$, with $\langle i_n \rangle$ the average noise current (so $i_n = i$ gives Poisson-based shot noise) and e the magnitude of the electron charge, $\langle i \rangle = \kappa$ NEP $= \sigma_i = \sqrt{2e\langle i_n \rangle}$, where κ (A/W) is the photodetector responsivity. Consider the thermal noise limit, and a dark current count rate of R electrons/s, resulting in NEP $= (e/\kappa)\sqrt{2R}$. We define a Poynting vector SNR $= S_d/\sigma_s$, where S_d is the Poynting vector magnitude (mean) at the detector and σ_s is the standard deviation, a reflection of the detector noise. Setting $\sigma_s = $ NEP$/A_e$, with A_e the effective detector aperture, gives a measure of detector noise. Based on achieved NEP and S_d for a typical laser source, we establish noise-based error bars on Poynting vector plots.

A typical NEP range for commercially available avalanche photodiodes (APDs) and photomultiplier tubes is $10^{-18} - 10^{-17}$ W/$\sqrt{\text{Hz}}$, and 10^{-22} W/$\sqrt{\text{Hz}}$ has been achieved for single-photon-counting detection with an APD operated at 78 K [80]. With $A_e = 10^{-12}$ m^2 and an assumed Poynting vector magnitude at the detector of $S_d = 10^{11}$ W/m^2, along with a NEP $= 10^{-17}$ W/$\sqrt{\text{Hz}}$, we find a SNR $= S_d A_e/$NEP $= 10^{16}$ or 160 dB - with the assumption of a 1 Hz electrical bandwidth. We choose a very conservative SNR of 40 dB in the simulations.

4.4   Results and Discussion

In Fig. 4.2, we plot S_x information measured by s_2 for both the PW and SI cases when the scatterers are located at $(0,0)$ for three different values of D. In Figs. 4.2(b) and (d), we show differences between the detector measurements for the three scatterer separations, using the $D = 0.02 \lambda$ case as a reference. Because of the relatively weak scatter, the measured data in Figs. 4.2(a) and (c) is very close to that

for the incident field alone. Figures 4.2(b) and (d) show error bars determined from $\sigma_s = S_d/\text{SNR} = 10^{-4}$, in other words, $\text{SNR} = 40$ dB. The end-to-end length of the error bars is equal to twice the standard deviation of the noise process. As expected, the 0.01λ change in D cannot be resolved by detectors with SNR=40 dB.
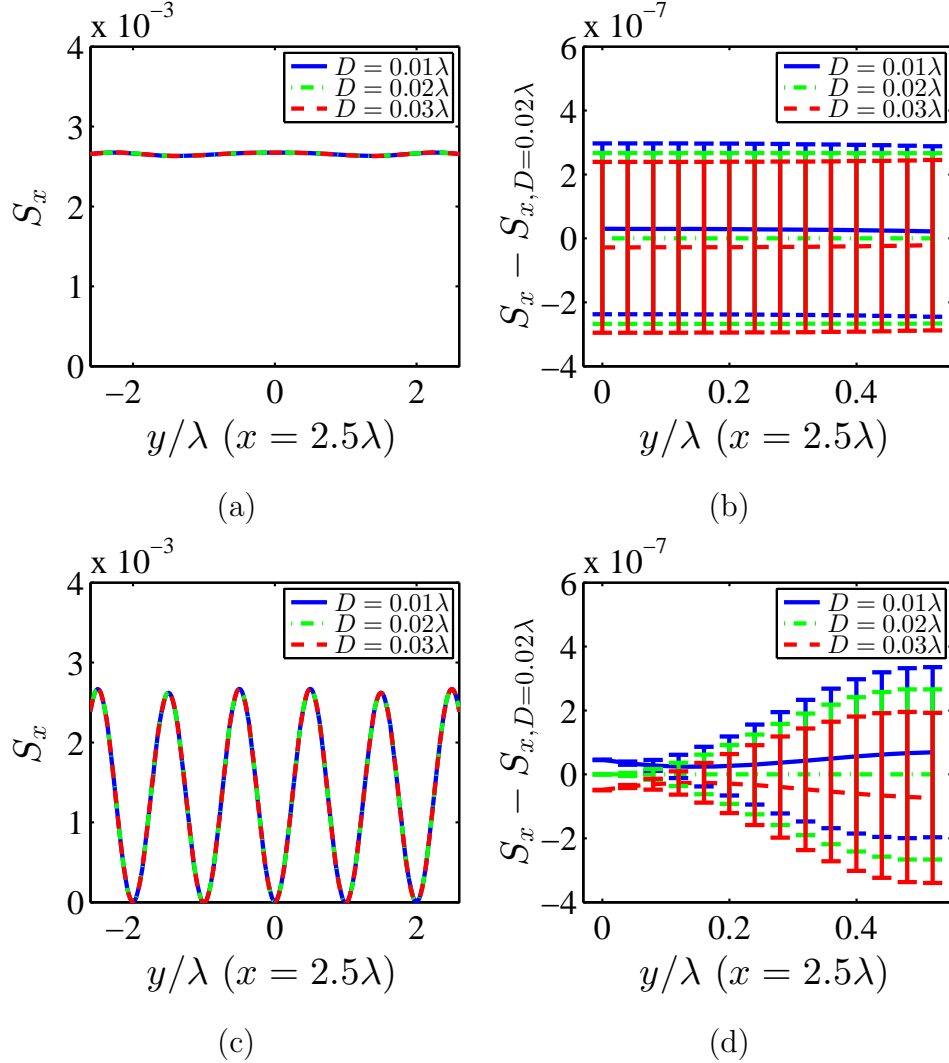
Fig. 4.2. Time-averaged Poynting vector in the $\hat{\mathbf{x}}$-direction, measured at s_2 for $D = 0.01\lambda$, 0.02λ, and 0.03λ, for the two $\epsilon_r = 1.5$ objects fixed at the center of the domain, $(0, 0)$. The spatial coordinates refer to the geometry in Fig. 4.1. The PW case is shown in (a) and (b), and the SI case is shown in (c) and (d). To clearly show the error bars, the data plotted in (b) and (d) is for $S_x - S_{x,D=0.02\lambda}$.

We use $(\Delta x, \Delta y)$ to represent the shift from the central, reference position of the two scatterers, $(0, 0)$. As the scatterers are scanned while preserving the geometry, the time-averaged Poynting vector measured at the detectors is compared with the Poynting vector data with the object at the reference position. Consider then the function

$$
\begin{aligned}
f(&\Delta x, \Delta y; D) \\
&= \int_{x,y \in \mathbf{s}} |\mathbf{S}(x, y; \Delta x, \Delta y, D) - \mathbf{S}(x, y; 0, 0, D)| \cdot d\mathbf{s},
\end{aligned}
\tag{4.3}
$$

which is the integral of the change in detected power due to motion over a surface (line) defined by $\mathbf{s}$ with a fixed scatterer separation, D. For the PW case, $\mathbf{s}$ includes only s_2, while for SI, $\mathbf{s}$ contains both s_1 and s_2. When noise is incorporated into the data, $f \to f_n$ in (4.3). Because the ranges of f and f_n are much greater than the small differences induced by the far-subwavelength change in D, we introduce

$$
g(\Delta x, \Delta y; D) = f_n(\Delta x, \Delta y; D) - f(\Delta x, \Delta y; D_0),
\tag{4.4}
$$

which reflects the change in D and in the detector data due to the motion of scatterers. Figure 4.3 shows $g(\Delta x, \Delta y; D)$, when the scatterers are scanned along the bottom $(\Delta y = -0.5\lambda)$ and left $(\Delta x = -0.5\lambda)$ boundaries, referring to Fig. 4.1, for $D_0 = 0.02\lambda$ and both the PW and SI cases. In Figs. 4.3(a) and (b), we see that the 0.01λ change in D is barely resolvable in $g(\Delta x, \Delta y; D)$ with a single incident plane wave and a 40 dB SNR. However, Figs. 4.3(c) and (d) show that the 0.01λ change in D can be easily resolved for the SI case. This resolution enhancement is due to the additional information encoded into the far-field scattered field (represented in the change in S_x and S_y) by the interaction between the scatterers and the structured illumination.

Based on the sensitivity that has now been established, we propose a method to determine the far-subwavelength distance between two scatterers as well as their dielectric constants. We use the notation $f(\Delta x, \Delta y; D, \epsilon_r)$ with an unknown dielectric constant for the scatterers. An experiment will yield $f_n(\Delta x, \Delta y; D, \epsilon_r)$ from far-field power measurements. Determination of the correct values of D and ϵ_r, denoted by
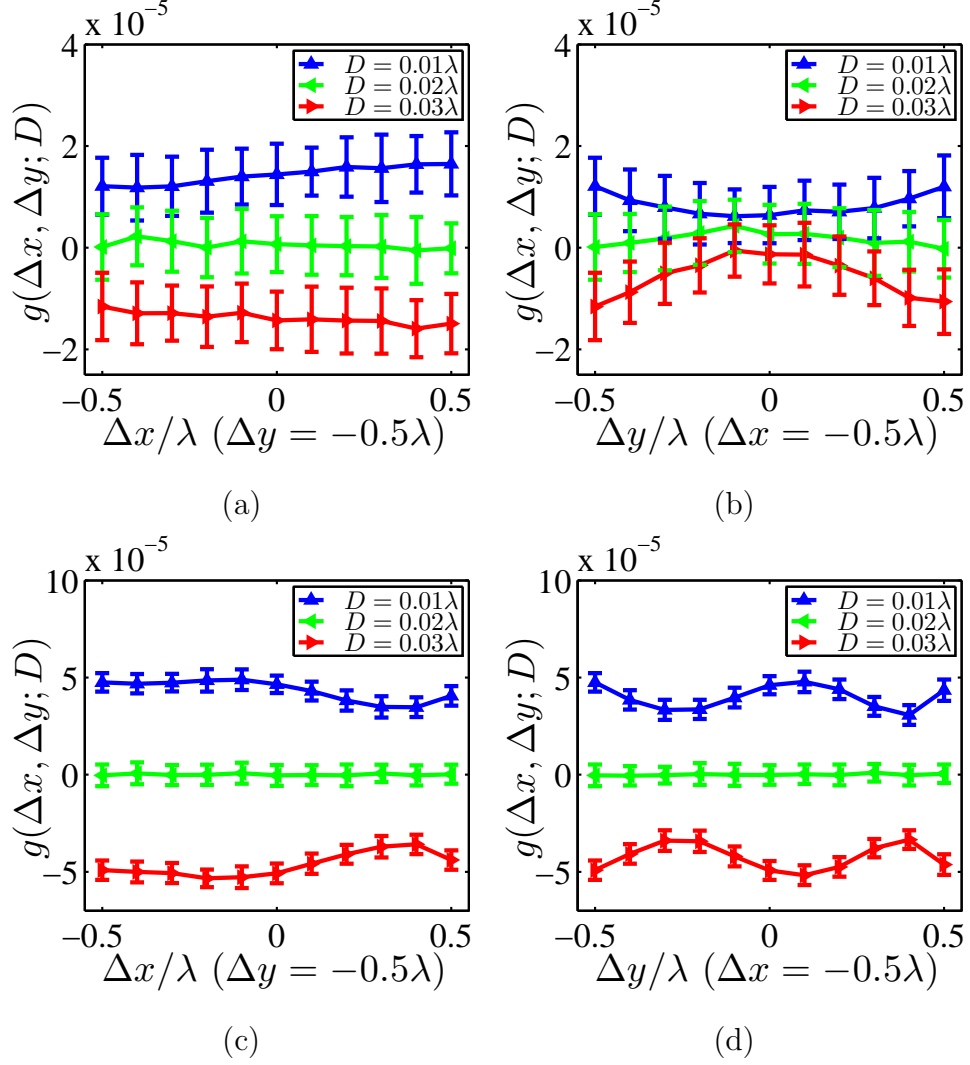
Fig. 4.3. Numerical values of $g(\Delta x, \Delta y; D)$ (see (4.4)) for the reference separation $D_0 = 0.02\lambda$ when the (two $\epsilon_r = 1.5$) scatterers are scanned along the (a) bottom and (b) left boundaries (the central region in Fig. 4.1(a)) for the PW case, and (c) and (d) for the SI situation, all with a SNR = 40 dB (producing the error bars).

D^* and ϵ_r^*, from the forward calculation of $f(\Delta x, \Delta y; D, \epsilon_r)$ for possible values of D and ϵ_r is achieved by minimizing the cost function

$$(D^*, \epsilon_r^*) = \underset{\{D, \epsilon_r\}}{\operatorname{argmin}} \sum_{\Delta x, \Delta y} |f_n(\Delta x, \Delta y; D, \epsilon_r) - f(\Delta x, \Delta y; D, \epsilon_r)|. \tag{4.5}$$
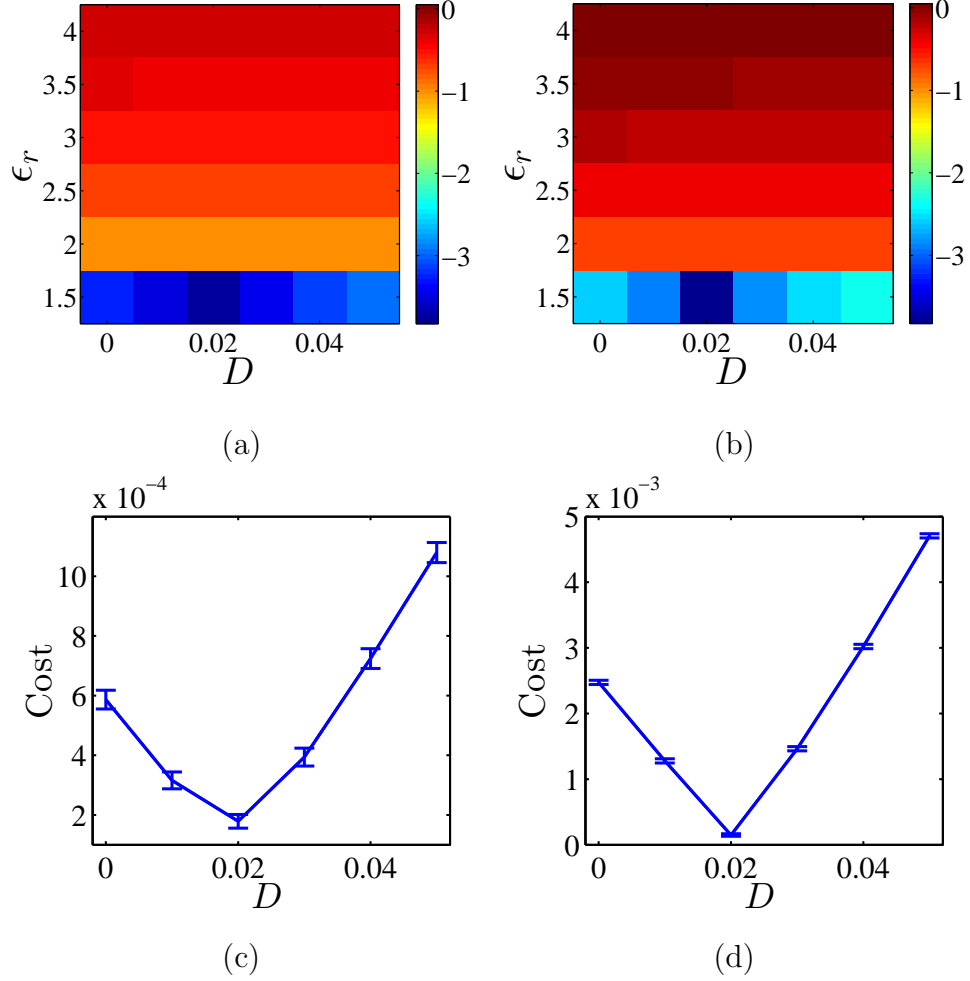
Fig. 4.4. Cost functions for a simulated experiment with $D^* = 0.02\lambda$ and $\epsilon_r^* = 1.5$. (a) and (b) are the decimal logarithm of the cost function for the PW and SI cases, respectively. (c) and (d) are plots of the costs for the correct value of ϵ_r for the PW and SI cases, respectively. The error bars give the standard deviation (estimated by performing the measurement 100 times) with SNR = 40 dB.

Figure 4.4 shows results from (4.5) for a hypothetical experiment with $D^* = 0.02\lambda$ and $\epsilon_r^* = 1.5$ for the PW (Fig. 4.4(a)) and SI (Fig. 4.4(b)) cases. The scatterers were scanned over a region of 0.5λ by 0.5λ to save computation time. Note that the minimum cost is with the correct separation and dielectric constant, despite the rather large SNR of 40 dB. We plot the cost at the correct ϵ_r as a function of D for the PW and SI cases in Figs. 4.4(c) and (d), respectively, in order to show the influence
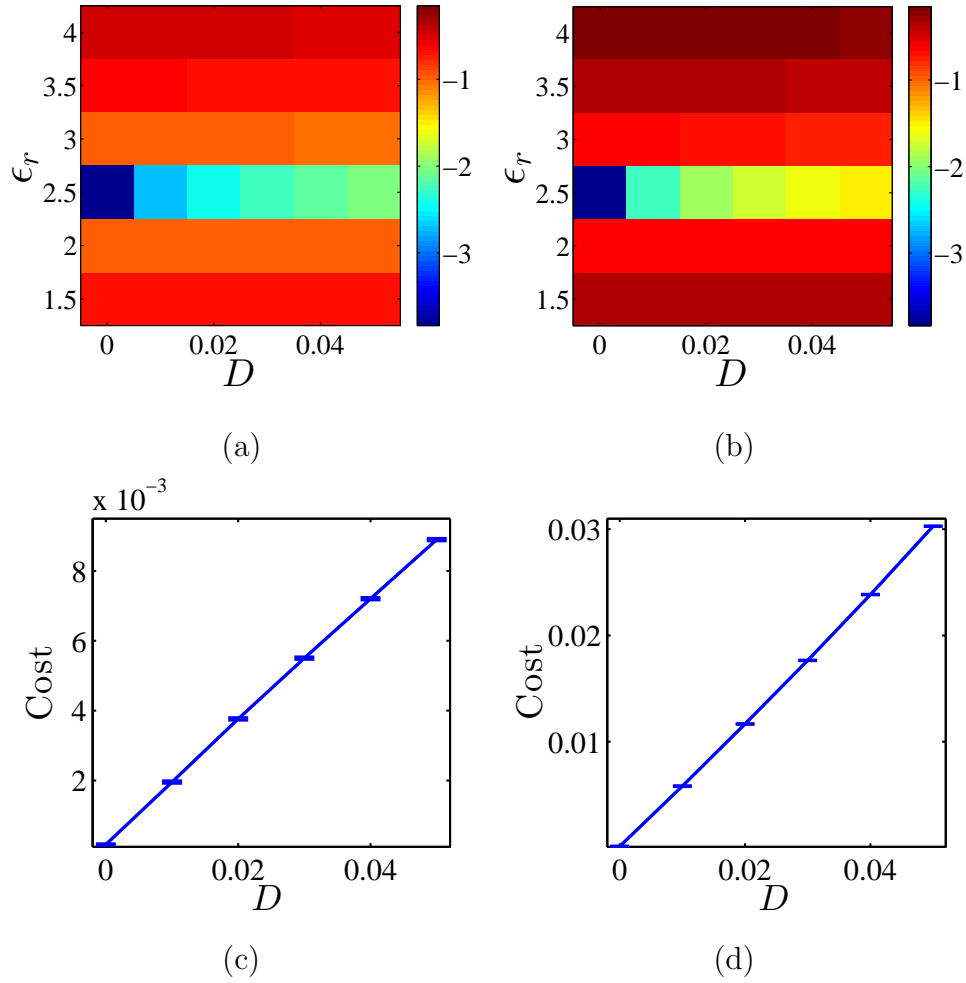
Fig. 4.5. Cost functions for a simulated experiment with $D^* = 0$ (a single object) and $\epsilon_r^* = 2.5$. The meaning of all sub-figures is the same as Fig. 4.4.

of detector noise in relation to the cost function features - as (barely noticeable) error bars. Notice that there is less sensitivity in the cost to variations in D for the PW case relative to that with SI. This is in agreement with the data presented in Figs. 4.3(a) and (b) (PW) relative to Figs. 4.3(c) and (d) (SI). Figure 4.5 shows results from another hypothetical experiment with $D^* = 0$ (a single scatterer) and $\epsilon_r^* = 2.5$. The method clearly works with $D^* = 0$, meaning that it is possible to distinguish one large scatterer from two smaller scatterers.

4.5 Conclusion

We have presented a far-subwavelength imaging method based on motion in structured light in two dimensions that can easily be extended to the three-dimensional case. Three or more beams would provide suitable illumination in which to move the object. The sensitivity of the measurement data to subwavelength scale object features is related to the structure of the incident field. Precise spatial scanning of the object is possible with piezoelectric stages that are routinely used in atomic force microscopy. Given wavelength-scale structure in the field, and the possible stage motion and detector noise, it appears that a spatial resolution on the order of 1 nm should be achievable with visible light. While we show that objects can be uniquely identified based on comparison with reference measurement data, use of a cost function imaging method [81] will in principle allow images to be reconstructed without pre-computed information. However, the data set in relation to regularization will have to be investigated. The structured illumination could be periodic, as we considered, or of some other form, such as speckle. Regardless, measured data can be taken with and without the object, and as a function of scan position.

5. ENHANCED AND TUNABLE RESOLUTION FROM AN IMPERFECT NEGATIVE REFRACTIVE INDEX LENS[†]

5.1 Introduction

Microscopy that can allow subwavelength or super resolution imaging is important in the physical, chemical, and biological sciences. However, the resolution of traditional far-field imaging systems is ultimately limited by $\lambda/(2\text{NA})$, where λ is the wavelength of the illumination and NA is the numerical aperture [12]. The fundamental reason for the existence of this diffraction limit is the exponential decay of the evanescent fields, leaving only the propagating part of the plane wave expansion of the scattered field from the object. It is the evanescent field portion of the spectrum that contains information about the subwavelength features of the object. In the far field, the evanescent field information is usually below the noise floor of the detector, making recovery of subwavelength information infeasible.

It has been proposed that a slab of negative refractive index material with negative permittivity and negative permeability can be used to focus both propagating and evanescent fields, making a perfect lens with infinite resolution [22]. A medium made of negative refractive index material is referred as a left-handed (LH) medium because the electric field, magnetic field, and the wave vector form a left-handed triplet. A medium made of positive refractive index material is therefore a right-handed (RH) medium for similar reasons. Unfortunately, a perfect negative refractive index medium does not exist in nature, and engineering such material is fundamentally limited by the intrinsic loss in practical materials as well as the need for a magnetic

material response at optical frequencies [82]. The presence of loss has restricted the operation of the LH slab lens to the near field [83], and the resolution of such a lens has been shown to be greatly compromised [24, 84]. A thin silver layer has been used to image down to a resolution of $\lambda/6$ [85]. However, this lens operates in the electrostatic limit [22], with small offset distance between the object and image planes. To date, there is no proposed operation of a true negative refractive index lens using conceivable nanostructured materials that could provide far-subwavelength resolution.

In this Letter, we present the possibility of improving the resolution of a LH slab lens by control of the material properties when both the object medium and the image medium have loss. We find that the transmittance of a LH slab lens at a particular spatial frequency can be greatly enhanced when the permittivity and permeability in the slab are complex. Tuning the imaginary parts of the permittivity and permeability for a series of spatial frequencies allows reconstruction of the evanescent part of the spatial frequency spectrum of the object field, and hence the recovery of subwavelength features of the object beyond the capability of a LH slab lens with fixed material parameters. The practicality of our proposal is presented following a discussion of the relevant issues.

5.2   Theory

Figure 5.1 shows the imaging geometry we consider, where each region is described by a relative permittivity $\epsilon_{ri} = \epsilon_i/\epsilon_0 = \epsilon'_{ri} + j\epsilon''_{ri}$ and a relative permeability $\mu_{ri} = \mu_i/\mu_0 = \mu'_{ri} + j\mu''_{ri}$, with $i = 1, 2, 3$ designating the region index from left to right. Assuming $\exp{(j\omega t)}$ dependence, the transmission coefficient from the object plane to the image plane can be obtained from the transverse transmission matrix method [86] as

$$T = \frac{(1 + r_{12})(1 + r_{23})e^{-j(k_{z1}d_1 + k_{z2}d_2 + k_{z3}d_3)}}{1 + r_{12}r_{23}e^{-j2k_{z2}d_2}}, \tag{5.1}$$

where $k_{zi} = k'_{zi} + jk''_{zi}$ describes the field variation in the positive $\hat{\mathbf{z}}$-direction in Medium i and r_{mn} is the reflection coefficient of the field incident onto the semi-
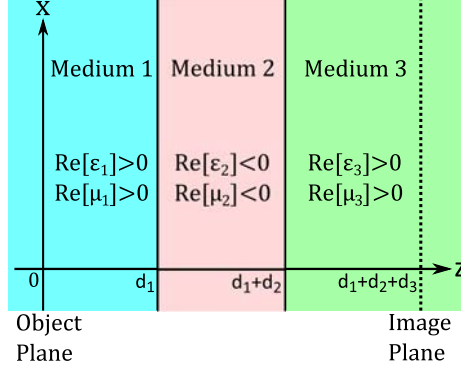
Fig. 5.1. The imaging geometry consists of three media indexed by $i = 1, 2, 3$ from left to right. Medium 1 is the RH object space; Medium 2 is the LH slab with thickness d_2; and Medium 3 is the RH image space. The distance between the object plane and the left boundary of the slab is d_1, and the distance between the image plane and the right boundary of the slab is d_3.

infinite Medium n from Medium m. Because of the time dependence assumed, both k'_{z1} and k'_{z3} are positive. In a LH medium, energy and wavefront travel in opposite directions, so $k'_{z2} < 0$. The longitudinal and transverse wavevectors are related by

$$
\begin{aligned}
k_{zi} &= k_0 \sqrt{\mu_{ri}\epsilon_{ri} - (k_x/k_0)^2} \\
&= k_0 \sqrt{\mu'_{ri}\epsilon'_{ri} - \mu''_{ri}\epsilon''_{ri} - (k_x/k_0)^2 + j(\mu'_{ri}\epsilon''_{ri} + \epsilon'_{ri}\mu''_{ri})}.
\end{aligned}
\tag{5.2}
$$

Deep into the evanescent spectrum ($|k_x/k_0| \gg 1$), the real part under the square root in (5.2) dominates, so that $|k''_{zi}| \gg |k'_{zi}|$.

The transmission coefficient in (5.1) can be greatly enhanced if $|r_{12}| \to \infty$ and/or $|r_{23}| \to \infty$. When Medium 1 and Medium 3 are the same, the reflection coefficients are $r_{23} = -r_{12} = (Z_3 - Z_2)/(Z_3 + Z_2)$, where Z_i is the wave impedance in Medium i. We focus on r_{23} in the following. For $|r_{23}| \to \infty$, $Z_3 + Z_2 = 0$. We discuss the conditions for $Z_3 + Z_2 = 0$ for both TE and TM polarizations without placing any restrictions on medium properties (allowing gain or loss) except their handedness. We will see that this provides very specific guidance on the material properties in Medium 2 and Medium 3.

For TM polarization, $Z_3 + Z_2 = 0$ gives

$$
\epsilon_2 k_{z3} + \epsilon_3 k_{z2} = 0. \tag{5.3}
$$

Substituting $\epsilon_2 = \epsilon_2' + j\epsilon_2''$, $\epsilon_3 = \epsilon_3' + j\epsilon_3''$, $k_{z2} = k_{z2}' + jk_{z2}''$, and $k_{z3} = k_{z3}' + jk_{z3}''$ into (5.3), we obtain

$$(\epsilon_3'k_{z2}' + \epsilon_2'k_{z3}' - \epsilon_3''k_{z2}'' - \epsilon_2''k_{z3}'') + j(\epsilon_3''k_{z2}' + \epsilon_2''k_{z3}' + \epsilon_3'k_{z2}'' + \epsilon_2'k_{z3}'') = 0. \qquad (5.4)$$

The real and imaginary parts of (5.4) must both be zero for $|r_{23}| \to \infty$, so we have

$$\epsilon_3''k_{z2}'' + \epsilon_2''k_{z3}'' = \epsilon_3'k_{z2}' + \epsilon_2'k_{z3}' \qquad (5.5)$$

$$\epsilon_3'k_{z2}'' + \epsilon_2'k_{z3}'' = -(\epsilon_3''k_{z2}' + \epsilon_2''k_{z3}'). \qquad (5.6)$$

For most materials, the loss or gain in ϵ is small so that $|\epsilon_i'| \gg |\epsilon_i''|$. Considering also $|k_{zi}''| \gg |k_{zi}'|$ in the deep evanescent spectral range, the quantities with large absolute values are all on the left of (5.6), while those with small absolute values are all on the right. Because $\epsilon_3' > 0$ and $\epsilon_2' < 0$, (5.6) holds only when $k_{z2}''k_{z3}'' > 0$, meaning that both Medium 2 and Medium 3 should have gain or loss simultaneously. We consider the more practical lossy case and choose $k_{z2}'' < 0$ and $k_{z3}'' < 0$. From the handedness of Medium 2 and Medium 3, the right side of (5.5) is negative. For loss in Medium 2 and Medium 3, the left side of (5.5) is negative only when at least one of ϵ_2'' and ϵ_3'' is positive (electric gain). However, the electric gain must be smaller than the magnetic loss so that the medium has overall loss.

TE polarization is the dual of TM polarization, and the condition for $r_{23} \to \infty$ can be found to be

$$(\mu_3'k_{z2}' + \mu_2'k_{z3}' - \mu_3''k_{z2}'' - \mu_2''k_{z3}'') + j(\mu_3''k_{z2}' + \mu_2''k_{z3}' + \mu_3'k_{z2}'' + \mu_2'k_{z3}'') = 0. \qquad (5.7)$$

The real and imaginary parts of (5.7) must be zero, so we obtain

$$\mu_3''k_{z2}'' + \mu_2''k_{z3}'' = \mu_3'k_{z2}' + \mu_2'k_{z3}' \qquad (5.8)$$

$$\mu_3'k_{z2}'' + \mu_2'k_{z3}'' = -(\mu_3''k_{z2}' + \mu_2''k_{z3}'). \qquad (5.9)$$

The conditions for (5.8) and (5.9) to hold are also duals of the TM case. As for TM, it is practical to assume that both Medium 2 and Medium 3 have loss. However, at least one of μ_2'' and μ_3'' must be positive (magnetic gain) for (5.8) to hold. The magnetic gain, however, must be smaller than the electric loss so that the medium has overall loss.

5.3 Numerical Results

Consider now the implications of the above LH lens analysis. The usual situation is that Medium 1 would be non-magnetic with some electric loss, for example, a biological molecule. If Medium 3 were magnetic, then control of the electric and magnetic properties in this region could be used to compensate for imperfect lens parameters, allowing a large $|r_{23}|$. If we assume that Medium 3 is non-magnetic, the only opportunity for achieving large $|r_{23}|$ is to have a magnetic material response in Medium 2, consistent with the LH lens operation. For TE polarization, Medium 2 needs to have large electric loss and small magnetic gain. For TM polarization, Medium 2 should have small electric gain and large magnetic loss. In addition, we consider the case where the real parts of ϵ_{ri} and μ_{ri} are matched and for vacuum. The material properties can then be written as $\epsilon_{r1} = 1 + j\epsilon_{r1}''$, $\mu_{r1} = 1$, $\epsilon_{r2} = -1 + j\epsilon_{r2}''$, $\mu_{r2} = -1 + j\mu_{r2}''$, $\epsilon_{r3} = 1 + j\epsilon_{r3}''$, and $\mu_{r3} = 1$. With fixed ϵ_{r1}'' and ϵ_{r3}'', both negative for loss, there are two free variables to satisfy (5.4) or (5.7), ϵ_{r2}'' and μ_{r2}''. However, an exact solution to these equations may not exist, and the amount of gain and loss achievable in material engineering is limited, Therefore, it is more practical to specify a range for ϵ_{r2}'' and μ_{r2}'' and then find the maximum $|r_{23}|$. We vary both ϵ_{r2}'' and μ_{r2}'' over three orders of magnitude (10^{-4} to 10^{-1}) in a numerical procedure to find their optimal values, denoted by $\epsilon_{r2}''^*$ and $\mu_{r2}''^*$, that give the maximum $|r_{23}|$ at a given k_x, for various losses in Medium 1 and Medium 3.

In Fig. 5.2, we plot the magnitude of the transmittance (5.1) for the evanescent spectrum on a log scale when Medium 1 and 3 are lossy, for both TE (Figs. 5.2 (a) and (b)) and TM (Figs. 5.2 (c) and (d)) polarizations for $d_2 = 2d_1 = 2d_3 = 0.25\lambda$ (see Fig. 5.1). When all three media are lossless, the lens is perfect, and $T(k_x/k_0) = 1$ for all k_x We optimize Medium 2 properties to maximize $|r_{23}|$ at $k_x/k_0 = 10$, and the corresponding transmittance peak is obvious in all four cases. We also list the engineered Medium 2 properties and the optimized transmittance $|T^*|$ for both TE (Table 5.1) and TM (Table 5.2) polarizations for $k_x/k_0 = 8, 10, 12$. As a reference, we show the result for $\epsilon_{r2}'' = \epsilon_{r3}''$ and $\mu_{r2}'' = 0$ as $|T^L|$ in Tables 5.1 and 5.2
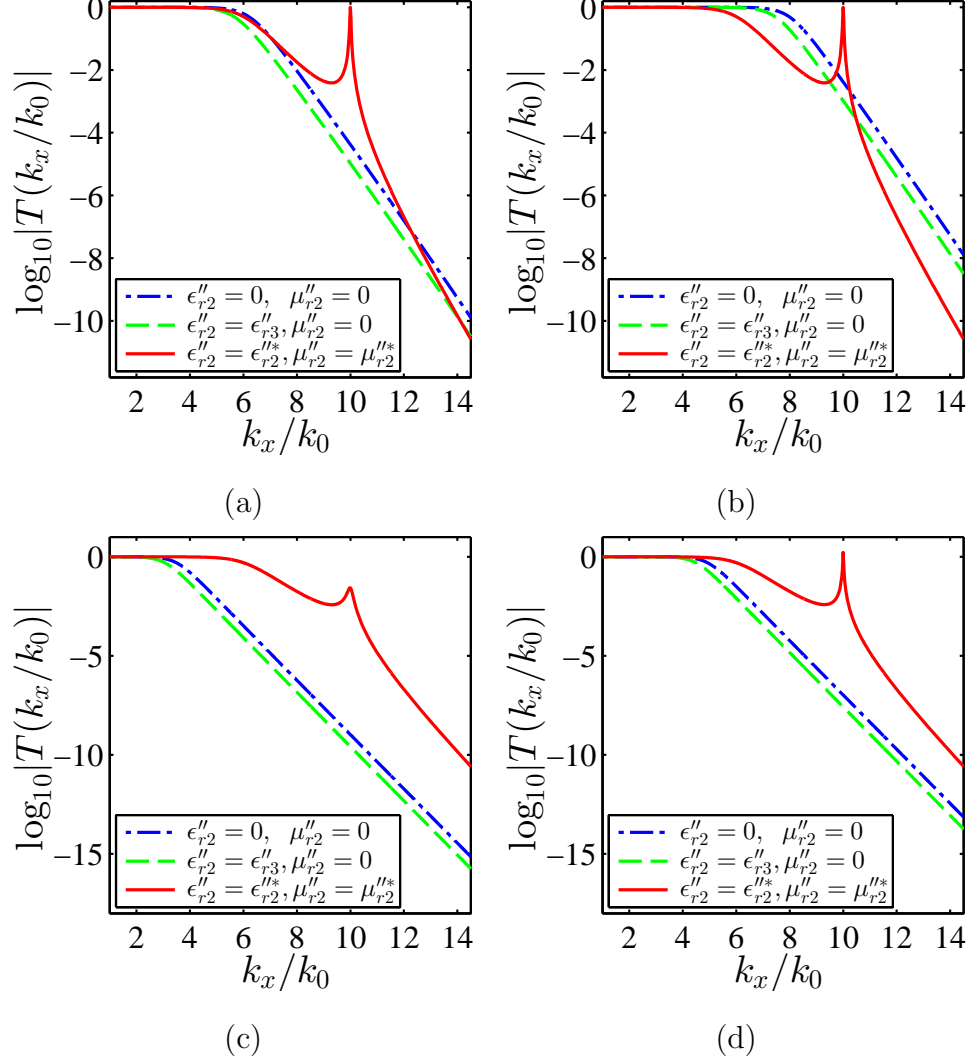
Fig. 5.2. Plot of $\log_{10}|T(k_x/k_0)|$ when Medium 2 is lossless ($\epsilon''_{r2} = 0$, $\mu''_{r2} = 0$), has electric loss ($\epsilon''_{r2} = \epsilon''_{r3}$, $\mu''_{r2} = 0$), and is optimized for $k_x/k_0 = 10$ ($\epsilon''_{r2} = \epsilon''^*_{r2}$, $\mu''_{r2} = \mu''^*_{r2}$): (a) $\epsilon''_{r1} = \epsilon''_{r3} = -0.01$, TE polarization; (b) $\epsilon''_{r1} = \epsilon''_{r3} = -0.001$, TE polarization; (c) $\epsilon''_{r1} = \epsilon''_{r3} = -0.01$, TM polarization; and (d) $\epsilon''_{r1} = \epsilon''_{r3} = -0.001$, TM polarization. Referring to Fig. 5.1, $d_2 = 2d_1 = 2d_3 = 0.25\lambda$. Note that the green dashed line corresponds to the situation for T^L in Tables 5.1 and 5.2.

to illustrate the importance of the control of the lens material properties. Note from Table 5.1 that μ''^*_{r2} is at the minimum of the allowed values, indicating only a small magnetic gain is sufficient. Note also that the requirement for small magnetic gain is a consequence of Medium 3 being non-magnetic. Table 5.2 shows that $|T^L|$ falls below 10^{-4} even for relatively small k_x/k_0 and that an engineered Medium 2 can produce

a significantly large $|T^*|$ in most cases. Given the ability to increase the evanescent field transmittance at a certain spatial frequency, we propose a method to image the far-subwavelength features of an object.

$\epsilon_{r1}'', \epsilon_{r3}''$	k_x/k_0	$\epsilon_{r2}''^*$	$\mu_{r2}''^*$	$|T^*|$	$|T^L|$
-0.01	8	-0.0027	0.0001	1.0000	0.0023
-0.01	10	-0.0099	0.0001	1.0010	1.0×10^{-5}
-0.01	12	-0.0187	0.0001	1.6034	4.0×10^{-8}
-0.001	8	-0.0117	0.0001	1.0000	0.1904
-0.001	10	-0.0189	0.0001	1.0003	0.0100
-0.001	12	-0.0277	0.0001	1.1763	4.0×10^{-6}

Table 5.1.
Values for the optimal parameters $\epsilon_{r2}''^*$ and $\mu_{r2}''^*$ and transmittance comparison for the TE polarization case. $|T^*|$ denotes the transmittance of the system when Medium 2 has been optimized to maximize $|r_{23}|$. $|T^L|$ is the case when Medium 2 has the same electric loss as Medium 1 and Medium 3 but with $\mu_{r2}'' = 0$.

$\epsilon_{r1}'', \epsilon_{r3}''$	k_x/k_0	$\epsilon_{r2}''^*$	$\mu_{r2}''^*$	$|T^*|$	$|T^L|$
-0.01	8	0.0101	-0.0127	1.0746	1.5×10^{-7}
-0.01	10	0.0101	-0.0199	0.0268	2.6×10^{-10}
-0.01	12	0.0101	-0.0287	4.8×10^{-5}	4.8×10^{-13}
-0.001	8	0.0011	-0.0127	1.0007	1.5×10^{-5}
-0.001	10	0.0011	-0.0199	1.6702	2.6×10^{-8}
-0.001	12	0.0011	-0.0287	0.0046	4.8×10^{-11}

Table 5.2.
Values for the optimal parameters $\epsilon_{r2}''^*$ and $\mu_{r2}''^*$ and transmittance comparison for TM polarization. The variables are the same as for Table 5.1.

Consider an object field denoted by $O(x)$, and its spatial Fourier transform $\mathcal{O}(k_x) = \mathcal{F}\{O(x)\}$, where $\mathcal{F}$ is the Fourier transform operator. For a given LH slab lens, the image field $I(x)$ can be modeled by $I(x) = \mathcal{F}^{-1}\{T(k_x)\mathcal{O}(k_x)\}$, where $\mathcal{F}^{-1}$ is the

inverse Fourier transform operator. For TE (TM) polarization, $O(x)$ and $I(x)$ correspond to $E_y(x)$ ($H_y(x)$) at the object and image planes, respectively (Fig. 5.1). A perfect lens would have $T(k_x) = 1$ for all k_x, hence the image would be identical to the object. For physical materials with even a small amount of loss, $T(k_x)$ is complex and decays significantly as k_x grows [83], as shown in Fig. 5.2 (blue and green lines). If exact and noise-free field measurements can be made at the image plane and $T(k_x)$ is known, the object field can be obtained from inverting the effect of the lens $O(x) = \mathcal{F}^{-1}\{\mathcal{I}(k_x)/T(k_x)\}$, where $\mathcal{I}(k_x) = \mathcal{F}\{I(x)\}$. Unfortunately, the high spatial frequency components can be easily buried in the measurement due to noise, making the inversion impossible.

The higher spatial frequency information in the object is retrievable as long as it is above the noise floor of the detector. For good detectors [80], a signal-to-noise ratio (S/N) of 60 dB is not difficult to achieve. However, this S/N is measured with respect to the Poynting vector and not a particular spatial frequency component of the field. With this in mind, we propose the following scheme to calculate the spatial frequency spectrum of the object and hence determine the object in the presence of noise. The propagating spatial frequency information of the object is easy to obtain, and variations in the image geometry and materials can be compensated. For a certain evanescent spatial frequency $k_x^\alpha > k_0$, we optimize Medium 2 such that $|T(k_x = k_x^\alpha)|$ is maximized. We denote T by T^* when Medium 2 has the optimal free parameters. If $|T^*(k_x^\alpha)| \geq 10^{-3}$, corresponding to a threshold associated with a 60 dB S/N, we add noise to the image in the spatial domain and denote the noisy image by $I_n(x)$. We assume that at each detector position x the noise process is a circular Gaussian random variable in the complex plane whose standard deviation is equal to 10^{-3} of $|I(x)|$, which roughly relates to a 60 dB S/N. The reconstructed object spectrum at k_x^α can be computed as $\mathcal{O}^*(k_x^\alpha) = \mathcal{I}_n(k_x^\alpha)/T^*(k_x^\alpha)$. We form $\mathcal{O}^*$ this way for increasing k_x^α until $|T^*(k_x^\alpha)| < 10^{-3}$. The reconstructed object, $O^*(x)$, is the inverse Fourier transform of $\mathcal{O}^*(k_x)$.
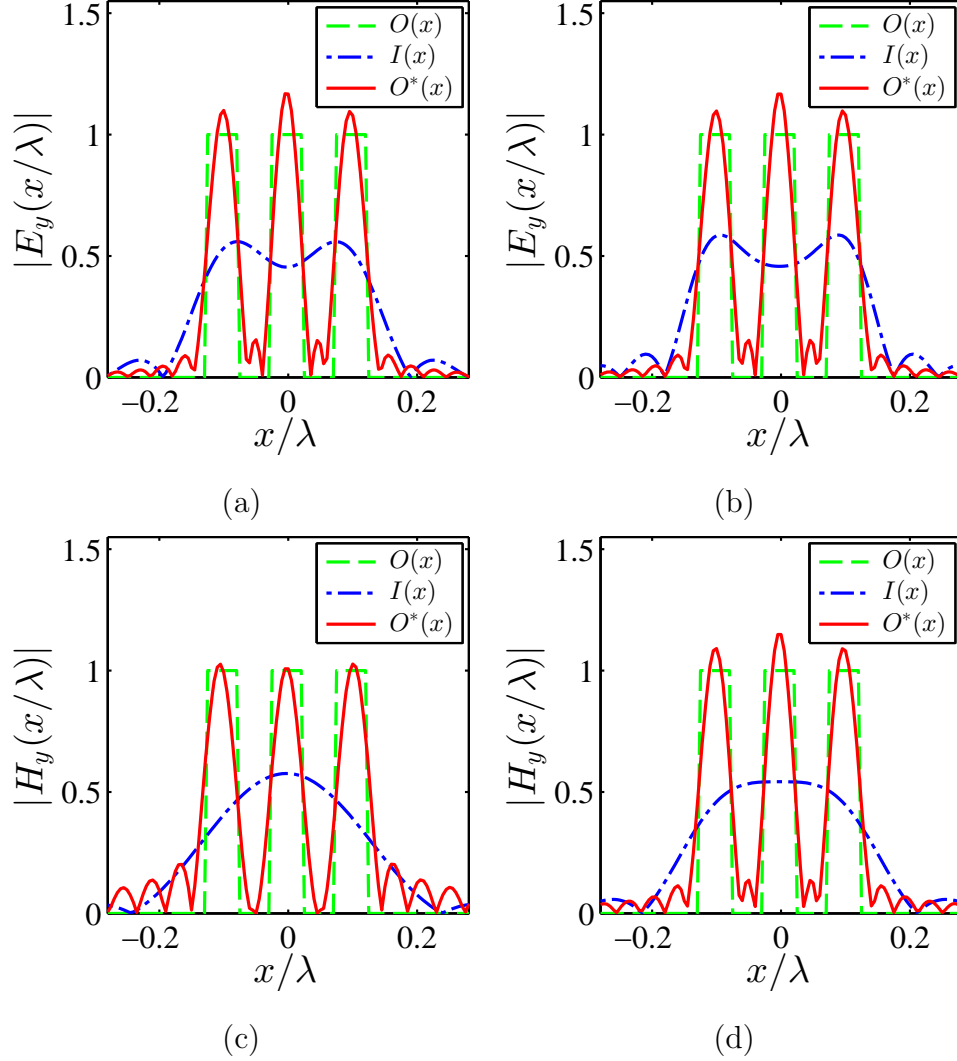
Fig. 5.3. Plot of the object, $O(x)$, LH slab lens image, $I(x)$, and the reconstructed image through Medium 2 optimization, $O^*(x)$ for: (a) $\epsilon''_{r1} = \epsilon''_{r3} = -0.01$, TE polarization; (b) $\epsilon''_{r1} = \epsilon''_{r3} = -0.001$, TE polarization; (c) $\epsilon''_{r1} = \epsilon''_{r3} = -0.01$, TM polarization; and (d) $\epsilon''_{r1} = \epsilon''_{r3} = -0.001$, TM polarization.

Figure 5.3 shows the LH slab lens image and the reconstructed image of a triple slit object having 0.05λ slits and 0.05λ edge-to-edge separation. The TE polarized field is better imaged by the LH slab lens than the TM case because $|T(k_x)|$ for large k_x is larger for TE polarization (see Fig. 5.2). The blue dashed-dotted response is the case with $T = T^L$, without optimization, and the slits cannot be resolved by the lossy LH slab lens in all cases. When Medium 2 is optimized and the object is reconstructed

according to our proposed method, good images of the object are obtained for both TE and TM polarizations. This demonstrates the potential of our method to image far-subwavelength structures when the object and image domains are lossy.

5.4 Conclusion

We have proposed a method to enhance the deep evanescent spectral information at the image plane by engineering the negative refractive index lens material parameters for the practical situation where the object and image domains have loss, and the lens has overall loss. The approach requires measurement of field data, facilitated by an interferometer. This method provides access to subwavelength information about the object field under the assumption that Medium 1 and Medium 3 are known, leading to an engineered response for the lens as a function of k_x. Although fine tuning of loss and gain in the LH medium may not be easy, one can anticipate that new methods and metamaterials will be developed to allow such control. While a single set of material parameters could be used to enhance the resolution, better results require adjustment to optimize the result at specific k_x during the experiment. Finally, the case that we considered had a relatively thin lens and stand-off distance from the object. It may be possible to increase this, depending on the material parameters involved or the lens configuration. However, the likely situation is that this approach will be effective only over relatively small length scales, on the order of a wavelength or so, leading to expectations for imaging small objects or larger objects (like cells) to such a depth.

6. SUMMARY

An analytical probability density function that is able to describe field statistics in a broad spectrum of wave transport regimes has been derived. This new field density function is developed under the assumption that the field can be modeled as a random phasor sum of a random number of contributing phasors. This new field probability density function and the well-known K-distribution for wave intensity are coherent statistical descriptions that unveil the intrinsic connection between intensity and field. Because both contain Bessel functions, the term "circular Bessel statistics" is used to refer to both density functions. Numerical simulations of electromagnetic waves propagating in 2D random media confirm that our new density function can be applied to the total field in the Anderson localization regime and the residual field in the weakly scattering regime. Having a set of density functions that work in a variety of scattering regimes provides a framework for better understanding of wave propagation in random media, facilitating random media characterization, design of random lasers, and imaging in and through scattering medium.

A non-fluorescent far-subwavelength imaging method that incorporates object motion with structured light illumination and far-field measurement data is proposed. Numerical simulations demonstrate that the proposed method can distinguish image features on the nanometer scale with visible light, even in the presence of generous detector noise. Another method is developed to image the far-subwavelength features of an object by reconstructing the evanescent part of its spectrum through engineering the material properties in the negative refractive index material lens. This approach works even in the presence of losses in the object and image media.

REFERENCES

REFERENCES

[1] J. W. Goodman, *Speckle Phenomena in Optics: Theory and Applications.* Roberts & Co, 2007.

[2] J. D. Rigden and E. I. Gordon, "Granularity of scattered optical maser light," *Proc. IRE*, vol. 50, no. 11, p. 2367, 1962.

[3] J. W. Goodman, *Statistical Optics.* Wiley, 2000.

[4] M. A. Webster, T. D. Gerke, K. J. Webb, and A. M. Weiner, "Spectral and temporal speckle field measurements of a random medium," *Opt. Lett.*, vol. 29, no. 13, pp. 1491–1493, July 2004.

[5] T. D. Gerke, M. A. Webster, A. M. Weiner, and K. J. Webb, "Frequency-resolved interferometer measurements of polarized wave propagation in scattering media," *J. Opt. Soc. Am. A*, vol. 22, no. 12, pp. 2691–2699, Dec 2005.

[6] K. Vynck, R. Pierrat, and R. Carminati, "Polarization and spatial coherence of electromagnetic waves in uncorrelated disordered media," *Phys. Rev. A*, vol. 89, p. 013842, Jan 2014.

[7] M. C. W. van Rossum and T. M. Nieuwenhuizen, "Multiple scattering of classical waves: microscopy, mesoscopy, and diffusion," *Rev. Mod. Phys.*, vol. 71, pp. 313–371, Jan 1999.

[8] P. W. Anderson, "Absence of diffusion in certain random lattices," *Phys. Rev.*, vol. 109, no. 5, pp. 1492–1505, 1958.

[9] E. Akkermans and G. Montambaux, *Mesoscopic Physics of Electrons and Photons.* Cambridge University Press, 2007.

[10] K. Busch, C. M. Soukoulis, and E. N. Economou, "Transport and scattering mean free paths of classical waves," *Phys. Rev. B*, vol. 50, pp. 93–98, Jul 1994.

[11] E. Jakeman and P. N. Pusey, "Significance of k distributions in scattering experiments," *Phys. Rev. Lett.*, vol. 40, pp. 546–550, Feb 1978.

[12] E. Abbe, "Beiträge zur theorie des mikroskops und der mikroskopischen wahrnehmung," *Arch. Mikr. Anat.*, vol. 9, no. 1, pp. 413–418, 1873.

[13] S. F. Gibson and F. Lanni, "Experimental test of an analytical model of aberration in an oil-immersion objective lens used in three-dimensional light microscopy," *J. Opt. Soc. Am. A*, vol. 8, no. 10, pp. 1601–1613, Oct 1991.

[14] A. Gur, D. Fixler, V. Micó, J. Garcia, and Z. Zalevsky, "Linear optics based nanoscopy," *Opt. Express*, vol. 18, no. 21, pp. 22 222–22 231, Oct 2010.

[15] C. Barsi and J. W. Fleischer, "Nonlinear abbe theory," *Nature Photon.*, vol. 7, no. 8, pp. 639–643, 2013.

[16] J. Zhu, J. Christensen, J. Jung, L. Martin-Moreno, X. Yin, L. Fok, X. Zhang, and F. Garcia-Vidal, "A holey-structured metamaterial for acoustic deep-subwavelength imaging," *Nature Phys.*, vol. 7, no. 1, pp. 52–55, 2010.

[17] E. Mudry, K. Belkebir, J. Girard, J. Savatier, E. Le Moal, C. Nicoletti, M. Allain, and A. Sentenac, "Structured illumination microscopy using unknown speckle patterns," *Nature Photon.*, vol. 6, no. 5, pp. 312–315, 2012.

[18] B. Bailey, D. Farkas, D. Taylor, and F. Lanni, "Enhancement of axial resolution in fluorescence microscopy by standing-wave excitation," *Nature*, vol. 366, no. 6450, p. 44, 1993.

[19] S. W. Hell and J. Wichmann, "Breaking the diffraction resolution limit by stimulated emission: stimulated-emission-depletion fluorescence microscopy," *Opt. Lett.*, vol. 19, no. 11, pp. 780–782, Jun 1994.

[20] E. Betzig, G. H. Patterson, R. Sougrat, O. W. Lindwasser, S. Olenych, J. S. Bonifacino, M. W. Davidson, J. Lippincott-Schwartz, and H. F. Hess, "Imaging intracellular fluorescent proteins at nanometer resolution," *Science*, vol. 313, no. 5793, pp. 1642–1645, 2006.

[21] M. J. Rust, M. Bates, and X. Zhuang, "Sub-diffraction-limit imaging by stochastic optical reconstruction microscopy (storm)," *Nat. Methods*, vol. 3, no. 10, pp. 793–796, 2006.

[22] J. B. Pendry, "Negative refraction makes a perfect lens," *Phys. Rev. Lett.*, vol. 85, pp. 3966–3969, Oct 2000.

[23] K. J. Webb and M. Yang, "Subwavelength imaging with a multilayer silver film structure," *Opt. Lett.*, vol. 31, no. 14, pp. 2130–2132, Jul 2006.

[24] K. J. Webb, M. Yang, D. W. Ward, and K. A. Nelson, "Metrics for negative-refractive-index materials," *Phys. Rev. E*, vol. 70, p. 035602, Sep 2004.

[25] Z. Liu, S. Durant, H. Lee, Y. Pikus, N. Fang, Y. Xiong, C. Sun, and X. Zhang, "Far-field optical superlens," *Nano Lett.*, vol. 7, no. 2, pp. 403–408, 2007.

[26] Y. Xiong, Z. Liu, C. Sun, and X. Zhang, "Two-dimensional imaging by far-field superlens at visible wavelengths," *Nano Lett.*, vol. 7, no. 11, pp. 3360–3365, 2007.

[27] J. Rho, Z. Ye, Y. Xiong, X. Yin, Z. Liu, H. Choi, G. Bartal, and X. Zhang, "Spherical hyperlens for two-dimensional sub-diffractional imaging at visible frequencies," *Nature Commun.*, vol. 1, p. 143, 2010.

[28] Z. Zalevsky, "Nonlinear optics: Defying abbe's law," *Nature Photon.*, vol. 7, no. 8, pp. 593–594, 2013.

[29] N. Shnerb and M. Kaveh, "Non-rayleigh statistics of waves in random systems," *Phys. Rev. B*, vol. 43, pp. 1279–1282, Jan 1991.

[30] E. Kogan, M. Kaveh, R. Baumgartner, and R. Berkovits, "Statistics of waves propagating in a random medium," *Phys. Rev. B*, vol. 48, pp. 9404–9410, Oct 1993.

[31] E. Kogan and M. Kaveh, "Random-matrix-theory approach to the intensity distributions of waves propagating in a random medium," *Phys. Rev. B*, vol. 52, pp. R3813–R3815, Aug 1995.

[32] T. M. Nieuwenhuizen and M. C. W. van Rossum, "Intensity distributions of waves transmitted through a multiple scattering medium," *Phys. Rev. Lett.*, vol. 74, pp. 2674–2677, Apr 1995.

[33] E. Jakeman and P. N. Pusey, "A model for non-rayleigh sea echo," *IEEE Trans. Ant. Propag.*, vol. 24, no. 6, pp. 806–814, 1976.

[34] L. C. Andrews and R. L. Phillips, "Mathematical genesis of the i-k distribution for random optical fields," *J. Opt. Soc. Am. A*, vol. 3, no. 11, pp. 1912–1919, Nov 1986.

[35] V. S. R. Gudimetla and J. F. Holmes, "Probability density function of the intensity for a laser-generated speckle field after propagation through the turbulent atmosphere," *J. Opt. Soc. Am. A*, vol. 72, no. 9, pp. 1213–1218, Sep 1982.

[36] J. H. Churnside and R. J. Hill, "Probability density of irradiance scintillations for strong path-integrated refractive turbulence," *J. Opt. Soc. Am. A*, vol. 4, no. 4, pp. 727–733, Apr 1987.

[37] L. C. Andrews, R. L. Phillips, and B. K. Shivamoggi, "Relations of the parameters of the i-k distribution for irradiance fluctuations to physical parameters of the turbulence," *Appl. Opt.*, vol. 27, no. 11, pp. 2150–2156, Jun 1988.

[38] A. García-Martín, J. J. Sáenz, and M. Nieto-Vesperinas, "Spatial field distributions in the transition from ballistic to diffusive transport in randomly corrugated waveguides," *Phys. Rev. Lett.*, vol. 84, pp. 3578–3581, Apr 2000.

[39] E. Jakeman, "On the statistics of k-distributed noise," *J. Phys. A*, vol. 13, no. 1, pp. 31–48, 1980.

[40] C. P. Lapointe, P. Zakharov, F. Enderli, T. Feurer, S. E. Skipetrov, and F. Scheffold, "Numerical study of anderson localization of terahertz waves in disordered waveguides," *Europhys. Lett.*, vol. 105, no. 3, p. 34002, 2014.

[41] E. Abrahams, P. W. Anderson, D. C. Licciardello, and T. V. Ramakrishnan, "Scaling theory of localization: Absence of quantum diffusion in two dimensions," *Phys. Rev. Lett.*, vol. 42, no. 10, pp. 673–676, 1979.

[42] A. A. Chabanov, M. Stoytchev, and A. Z. Genack, "Statistical signatures of photon localization," *Nature*, vol. 404, no. 6780, pp. 850–853, 2000.

[43] S. Zhang, B. Hu, P. Sebbah, and A. Z. Genack, "Speckle evolution of diffusive and localized waves," *Phys. Rev. Lett.*, vol. 99, no. 6, p. 063902, 2007.

[44] F. Riboli, P. Barthelemy, S. Vignolini, F. Intonti, A. De Rossi, S. Combrie, and D. S. Wiersma, "Anderson localization of near-visible light in two dimensions," *Opt. Lett.*, vol. 36, no. 2, pp. 127–129, 2011.

[45] M. Stoytchev and A. Z. Genack, "Measurement of the probability distribution of total transmission in random waveguides," *Phys. Rev. Lett.*, vol. 79, pp. 309–312, Jul 1997.

[46] H. Hu, A. Strybulevych, J. H. Page, S. E. Skipetrov, and B. A. van Tiggelen, "Localization of ultrasound in a three-dimensional elastic network," *Nature Phys.*, vol. 4, no. 12, pp. 945–948, 2008.

[47] D. J. Thouless, "Maximum metallic resistance in thin wires," *Phys. Rev. Lett.*, vol. 39, pp. 1167–1169, Oct 1977.

[48] S. A. van Langen, P. W. Brouwer, and C. W. J. Beenakker, "Nonperturbative calculation of the probability distribution of plane-wave transmission through a disordered waveguide," *Phys. Rev. E*, vol. 53, pp. R1344–R1347, Feb 1996.

[49] J. C. M. Garnett, "Colours in metal glasses and in metallic films," *Phil. Trans. R. Soc. A*, vol. 205, pp. 237–288, 1906.

[50] P. Mallet, C. A. Guérin, and A. Sentenac, "Maxwell-garnett mixing rule in the presence of multiple scattering: Derivation and accuracy," *Phys. Rev. B*, vol. 72, p. 014205, Jul 2005.

[51] J. B. Pendry, "Quasi-extended electron states in strongly disordered systems," *J. Phys. C*, vol. 20, no. 5, pp. 733–742, 1987.

[52] A. D. Stone, P. A. Mello, K. A. Muttalib, and J.-L. Pichard, "Random matrix theory and maximum entropy models for disordered conductors," in *Mesoscopic Phenomena in Solids*, B. L. Altshuler, P. A. Lee, and R. A. Webb, Eds. North-Holland, Amsterdam, 1991.

[53] A. D. Mirlin, "Distribution of local density of states in disordered metallic samples: Logarithmically normal asymptotics," *Phys. Rev. B*, vol. 53, pp. 1186–1192, Jan 1996.

[54] P. Peier, H. Merbold, V. Pahinin, K. A. Nelson, and T. Feurer, "Imaging of thz waves in 2d photonic crystal structures embedded in a slab waveguide," *New J. Phys.*, vol. 12, p. 013014, 2010.

[55] I. Reed, "On a moment theorem for complex gaussian processes," *IRE Trans. Inf. Theory*, vol. 8, no. 3, pp. 194–195, 1962.

[56] S. Barkhofen, J. J. Metzger, R. Fleischmann, U. Kuhl, and H.-J. Stöckmann, "Experimental observation of a fundamental length scale of waves in random media," *Phys. Rev. Lett.*, vol. 111, p. 183902, Nov 2013.

[57] H. Cao, Y. G. Zhao, S. T. Ho, E. W. Seelig, Q. H. Wang, and R. P. H. Chang, "Random laser action in semiconductor powder," *Phys. Rev. Lett.*, vol. 82, pp. 2278–2281, Mar 1999.

[58] T. Hisch, M. Liertzer, D. Pogany, F. Mintert, and S. Rotter, "Pump-controlled directional light emission from random lasers," *Phys. Rev. Lett.*, vol. 111, p. 023902, Jul 2013.

[59] L. Allen and D. G. C. Jones, "An analysis of the granularity of scattered optical maser light," *Phys. Lett.*, vol. 7, no. 5, pp. 321–323, 1963.

[60] J. C. Ricklin and F. M. Davidson, "Atmospheric turbulence effects on a partially coherent gaussian beam: implications for free-space laser communication," *J. Opt. Soc. Am. A*, vol. 19, no. 9, pp. 1794–1802, 2002.

[61] H. Leung and T. Lo, "Chaotic radar signal processing over the sea," *IEEE J. Ocean. Eng.*, vol. 18, no. 3, pp. 287–295, 1993.

[62] X. Wang, Y. Pang, G. Ku, X. Xie, G. Stoica, and L. V. Wang, "Noninvasive laser-induced photoacoustic tomography for structural and functional in vivo imaging of the brain," *Nat. Biotechnol.*, vol. 21, no. 7, pp. 803–806, 2003.

[63] D. J. Stephens and V. J. Allan, "Light microscopy techniques for live cell imaging," *Science*, vol. 300, no. 5616, pp. 82–86, 2003.

[64] J. A. Newman, Y. Chen, and K. J. Webb, "Zero-mean circular bessel statistics and anderson localization," *Phys. Rev. E*, vol. 90, p. 022119, Aug 2014.

[65] M. Abramowitz and I. A. Stegun, *Handbook of Mathematical Functions: with Formulas, Graphs, and Mathematical Tables.* Dover Publications, 2012.

[66] P. A. Lee and T. V. Ramakrishnan, "Disordered electronic systems," *Rev. Mod. Phys.*, vol. 57, no. 2, pp. 287–337, 1985.

[67] E. Abrahams, *50 Years of Anderson Localization.* World Scientific Publishing Company Incorporated, 2010.

[68] R. L. Weaver, "Anderson localization of ultrasound," *Wave Motion*, vol. 12, no. 2, pp. 129–142, 1990.

[69] S. John, "Electromagnetic absorption in a disordered medium near a photon mobility edge," *Phys. Rev. Lett.*, vol. 53, no. 22, pp. 2169–2172, 1984.

[70] P. W. Anderson, "The question of classical localization: A theory of white paint," *Philos. Mag. B*, vol. 52, pp. 505–509, 1985.

[71] S. E. Skipetrov and I. M. Sokolov, "Absence of anderson localization of light in a random ensemble of point scatterers," *Phys. Rev. Lett.*, vol. 112, p. 023905, Jan 2014.

[72] F. Scheffold, R. Lenke, R. Tweer, and G. Maret, "Localization or classical diffusion of light?" *Nature*, vol. 398, no. 6724, pp. 206–207, 1999.

[73] V. Ntziachristos, "Going deeper than microscopy: the optical imaging frontier in biology," *Nat. Methods*, vol. 7, no. 8, pp. 603–614, 2010.

[74] A. A. Chabanov and A. Z. Genack, "Field distributions in the crossover from ballistic to diffusive wave propagation," *Phys. Rev. E*, vol. 56, pp. R1338–R1341, Aug 1997.

[75] B. Redding, S. F. Liew, R. Sarma, and H. Cao, "Compact spectrometer based on a disordered photonic chip," *Nature Photon.*, vol. 7, no. 9, pp. 746–751, 2013.

[76] R. Heintzmann and C. G. Cremer, "Laterally modulated excitation microscopy: improvement of resolution by using a diffraction grating," *Proc. SPIE*, vol. 3568, pp. 185–196, 1999.

[77] M. G. L. Gustafsson, "Surpassing the lateral resolution limit by a factor of two using structured illumination microscopy," *J. Microsc.*, vol. 198, no. 2, pp. 82–87, 2000.

[78] Z. Wang, I. S. Chun, X. Li, Z.-Y. Ong, E. Pop, L. Millet, M. Gillette, and G. Popescu, "Topography and refractometry of nanostructures using spatial light interference microscopy," *Opt. Lett.*, vol. 35, no. 2, pp. 208–210, Jan 2010.

[79] S. W. Hell, "Far-field optical nanoscopy," *Science*, vol. 316, no. 5828, pp. 1153–1158, 2007.

[80] M. Akiba, K. Tsujino, and M. Sasaki, "Ultrahigh-sensitivity single-photon detection with linear-mode silicon avalanche photodiode," *Opt. Lett.*, vol. 35, no. 15, pp. 2621–2623, Aug 2010.

[81] A. B. Milstein, S. Oh, J. S. Reynolds, K. J. Webb, C. A. Bouman, and R. P. Millane, "Three-dimensional Bayesian optical diffusion tomography with experimental data," *Opt. Lett.*, vol. 27, no. 2, pp. 95–97, January 2002.

[82] R. P. Feynman, *QED: The Strange Theory of Light and Matter.* Princeton University Press, 2006.

[83] V. A. Podolskiy and E. E. Narimanov, "Near-sighted superlens," *Opt. Lett.*, vol. 30, no. 1, pp. 75–77, Jan 2005.

[84] M. Yang and K. J. Webb, "Poynting vector analysis of a superlens," *Opt. Lett.*, vol. 30, no. 18, pp. 2382–2384, Sep 2005.

[85] N. Fang, H. Lee, C. Sun, and X. Zhang, "Sub-diffraction-limited optical imaging with a silver superlens," *Science*, vol. 308, no. 5721, pp. 534–537, 2005.

[86] R. E. Collin, *Field Theory of Guided Waves.* IEEE Press, 1991.

[87] A. Stone and P. Mello, "Random matrix theory and maximum entropy models for disordered conductors," *Mesoscopic Phenomena in Solids*, pp. 369–448, 1991.

APPENDICES

A. DERIVATION OF PROBABILITY DENSITY FUNCTIONS OF TOTAL TRANSMISSION COEFFICIENT USING RANDOM MATRIX THEORY

This appendix is mainly dedicated to provide a detailed derivation of (2.8) and (2.9).

A.1 Definitions

A.1.1 Fourier and Laplace Transforms

One dimensional Fourier transform:

$$F(\omega) = \int_{-\infty}^{\infty} e^{-i\omega x} f(x) dx, \tag{A.1}$$

and the corresponding inverse Fourier transform is:

$$f(x) = \frac{1}{2\pi} \int_{-\infty}^{\infty} e^{i\omega x} F(\omega) d\omega, \tag{A.2}$$

Now consider one dimensional Laplace transform:

$$F(s) = \int_{-\infty}^{\infty} e^{-sx} f(x) dx, \tag{A.3}$$

and the corresponding inverse transform:

$$f(x) = \frac{1}{2\pi i} \int_{-i\infty}^{i\infty} e^{sx} F(s) ds, \tag{A.4}$$

We can see that by replacing s with $i\omega$, the Fourier transform and Laplace transform are equivalent. When applied to probability theory, Laplace transform is more frequently used because of the fact that its form is closer to that of the moment generating function.

A.1.2   Some Basic Probability Theory

The moment generating function for a random variable x is:

$$E[e^{-sx}] = \int_{-\infty}^{\infty} e^{-sx} p(x) dx, \qquad (A.5)$$

where $p(x)$ is the probability density function of the random variable x. Expanding e^{-sx} in a series:

$$
\begin{aligned}
E[e^{-sx}] &= E[\sum_{n=0}^{\infty} \frac{(-sx)^n}{n!}] \\
&= \sum_{n=0}^{\infty} \frac{(-s)^n}{n!} \int_{-\infty}^{\infty} x^n p(x) dx \\
&= \sum_{n=0}^{\infty} \frac{(-s)^n}{n!} \langle x^n \rangle \\
&= 1 - s\langle x \rangle + \frac{s^2}{2} \langle x^2 \rangle - \frac{s^3}{6} \langle x^3 \rangle + ...
\end{aligned}
\qquad (A.6)
$$

Equation (A.5) can also be viewed as the Laplace transform of $p(x)$. Hence if the moment generating function is known, we can obtain $p(x)$ by an inverse Laplace transform of the moment generating function:

$$p(x) = \frac{1}{2\pi i} \int_{-i\infty}^{i\infty} e^{sx} E[e^{-sx}] ds \qquad (A.7)$$

A.2   Calculation of Some Important Equations

First I show explicitly how to obtain the moment generating function of the normalized total transmission coefficient $\hat{T}_a$, namely equation (10) of [31]. In equation (9) of [31] the authors have inexplicitly normalized T_a by its average g/N, so it should have read:

$$p(\hat{T}_a) = \frac{1}{2\pi i} \int_{-i\infty}^{i\infty} e^{s\hat{T}_a} E[e^{-s\hat{T}_a}] ds, \qquad (A.8)$$

where $\hat{T}_a \equiv T_a/\langle T_a \rangle = T_a/(g/N)$. The moment generating function for $\hat{T}_a$ can be calculated using equation (8) of [31] as:

$$
\begin{aligned}
E[e^{-s\hat{T}_a}] &= \int_0^\infty e^{-s\hat{T}_a} p(\hat{T}_a) d\hat{T}_a \\
&= \int_0^\infty e^{-s\hat{T}_a} p(T_a) dT_a \\
&= \int_0^\infty e^{-sT_a N/g} p(T_a) dT_a \\
&= \int_0^\infty dT_a e^{-sNT_a/g} \int d\{\tau\} p(\{\tau\}) \int dU \delta(T_a - \sum_\alpha |u_{a\alpha}|^2 \tau_\alpha) \\
&= \int d\{\tau\} p(\{\tau\}) \int dU \int_0^\infty e^{-sNT_a/g} \delta(T_a - \sum_\alpha |u_{a\alpha}|^2 \tau_\alpha) dT_a \\
&= \int d\{\tau\} p(\{\tau\}) \int e^{-\frac{sN}{g}\sum_\alpha |u_{a\alpha}|^2 \tau_\alpha} dU
\end{aligned}
\tag{A.9}
$$

Now using the fact that "to leading order in $1/N$ both real and imaginary components of $u_{a\alpha}$ are independently distributed gaussian random variables with zero mean and variance $1/(2N)$" [31], the integration with respect to all $u_{a\alpha}$'s can be carried out. Focus on just one particular $u_{a\alpha} \equiv x_{a\alpha} + iy_{a\alpha}$:

$$
\begin{aligned}
&\int e^{-\frac{sN}{g}(x_{a\alpha}^2 + y_{a\alpha}^2)\tau_\alpha} p(x_{a\alpha}, y_{a\alpha}) dx_{a\alpha} dy_{a\alpha} \\
&= \int e^{-\frac{sN}{g}(x_{a\alpha}^2 + y_{a\alpha}^2)\tau_\alpha} \frac{1}{2\pi\sigma^2} e^{-(x_{a\alpha}^2 + y_{a\alpha}^2)/(2\sigma^2)} dx_{a\alpha} dy_{a\alpha}
\end{aligned}
\tag{A.10}
$$

Now substitute in $\sigma^2 = 1/(2N)$ and change to polar coordinates ($x_{a\alpha} = r\cos\theta$, and $y_{a\alpha} = r\sin\theta$):

$$
\begin{aligned}
&\int e^{-\frac{sN}{g}(x_{a\alpha}^2 + y_{a\alpha}^2)\tau_\alpha} \frac{1}{2\pi\sigma^2} e^{-(x_{a\alpha}^2 + y_{a\alpha}^2)/(2\sigma^2)} dx_{a\alpha} dy_{a\alpha} \\
&= \int_0^{2\pi} d\theta \int_0^\infty dr e^{-\frac{sN}{g}r^2\tau_\alpha} \frac{1}{2\pi\sigma^2} e^{-r^2/(2\sigma^2)} \\
&= \int_0^\infty 2Nr e^{-Nr^2(1+s\tau_\alpha/g)} dr \\
&= \int_0^\infty e^{-Nr^2(1+s\tau_\alpha/g)} d(Nr^2) \\
&= \frac{1}{1+s\tau_\alpha/g}
\end{aligned}
\tag{A.11}
$$

With this result in hand, equation (A.9) becomes:

$$
\begin{aligned}
E[e^{-s\hat{T}_a}] &= \int d\{\tau\}p(\{\tau\}) \int e^{-\dfrac{sN}{g}\sum_\alpha |u_{a\alpha}|^2 \tau_\alpha} dU \\
&= \int \prod_{\alpha=1}^{N} \frac{1}{1+s\tau_\alpha/g} p(\{\tau\})d\{\tau\} \qquad\qquad\text{(A.12)} \\
&\equiv \langle \prod_{\alpha=1}^{N} \frac{1}{1+s\tau_\alpha/g} \rangle_\tau
\end{aligned}
$$

Then I show how to arrive at equation (12) of [31]. What is left to do is to carry out the average with respect to τ, which is related to the "charges" ν_α via $\tau_\alpha = 1/\cosh^2(\nu_\alpha/2)$. The probability density function of ν_α is assumed to be uniform [87]:

$$
p(\nu) = \begin{cases} g/2 & 0 \leq \nu \leq 2L/l, \\ 0 & \nu > 2L/l. \end{cases} \qquad\qquad\text{(A.13)}
$$

Then using $p(\tau)d\tau = p(\nu)d\nu$, the probability density function for τ can be obtained:

$$
\begin{aligned}
p(\tau) &= p(\nu)|\frac{d\nu}{d\tau}| \\
&= \frac{g}{2\tau\sqrt{1-\tau}}
\end{aligned} \qquad\qquad\text{(A.14)}
$$

Using (11) of [31], we convert the average of different τ_α's to the average of τ:

$$
\begin{aligned}
E[e^{-s\hat{T}_a}] &= e^{\ln\langle \prod_{\alpha=1}^{N} \frac{1}{1+s\tau_\alpha/g}\rangle_\tau} \\
&= e^{-\sum_{\alpha=1}^{N} \ln(1+s\tau_\alpha/g)} \\
&= e^{-g\int_0^1 \frac{\ln(1+s\tau_\alpha/g)}{2\tau\sqrt{1-\tau}}d\tau} \qquad\qquad\text{(A.15)} \\
&= e^{-g\ln^2(\sqrt{1+s/g}+\sqrt{s/g})}
\end{aligned}
$$

Equation (2.8) is simply the inverse Laplace transform of (A.15).

Equation (18) of [31] can be obtained by a Taylor series expansion of (A.15) about $s = 0$:

$$
E[e^{-s\hat{T}_a}] \approx 1 - s + (0.5 + 1/(3g))s^2 + O[s]^3 \qquad\qquad\text{(A.16)}
$$

Compare (A.16) with (A.6), we find out that $\langle\hat{T}_a\rangle = 1$, and $\langle\hat{T}_a^2\rangle = 1 + 2/(3g)$. Thus the variance of normalized total transmission coefficient is $\langle\hat{T}_a^2\rangle - \langle\hat{T}_a\rangle^2 = 2/(3g)$.

Finally I show how to get equation (15) of [31] from equation (4) in [31]. Equation (15) of [31] should read (taking into account all normalization that is not written explicitly in the original paper):

$$p(\hat{T}_{ab}) = \int_0^\infty \frac{1}{\hat{T}_a} e^{-\hat{T}_{ab}/\hat{T}_a} p(\hat{T}_a) d\hat{T}_a \tag{A.17}$$

Equation (4) of [31] should read:

$$\langle \hat{T}_{ab}^n \rangle = n! \langle \hat{T}_a^n \rangle \tag{A.18}$$

In order to see how (A.18) leads to (A.17), first consider the writing $p(\hat{T}_{ab})$ as the inverse Fourier transform of its moment generating function (cf. (A.6) and (A.7)):

$$
\begin{aligned}
p(\hat{T}_{ab}) &= \frac{1}{2\pi} \int_{-\infty}^\infty e^{i\omega \hat{T}_{ab}} E[e^{-i\omega \hat{T}_{ab}}] d\omega \\
&= \int_{-\infty}^\infty e^{i\omega \hat{T}_{ab}} \sum_{n=0}^\infty \frac{(-i\omega)^n}{n!} \langle \hat{T}_{ab}^n \rangle \frac{d\omega}{2\pi}
\end{aligned}
\tag{A.19}
$$

Now substitute (A.18) into (A.19):

$$
\begin{aligned}
p(\hat{T}_{ab}) &= \int_{-\infty}^\infty e^{i\omega \hat{T}_{ab}} \sum_{n=0}^\infty \frac{(-i\omega)^n}{n!} n! \langle \hat{T}_a^n \rangle \frac{d\omega}{2\pi} \\
&= \int_{-\infty}^\infty e^{i\omega \hat{T}_{ab}} \sum_{n=0}^\infty \frac{(-i\omega)^n}{n!} \left(\int_0^\infty u^n e^{-u} du \right) \left(\int_0^\infty \hat{T}_a^n p(\hat{T}_a) d\hat{T}_a \right) \frac{d\omega}{2\pi}
\end{aligned}
\tag{A.20}
$$

Rearrange terms and change the order of integration:

$$
\begin{aligned}
p(\hat{T}_{ab}) &= \int_{-\infty}^\infty e^{i\omega \hat{T}_{ab}} \int_0^\infty du\, e^{-u} \int_0^\infty \sum_{n=0}^\infty \frac{(-i\omega u \hat{T}_a)^n}{n!} p(\hat{T}_a) d\hat{T}_a \frac{d\omega}{2\pi} \\
&= \int_{-\infty}^\infty e^{i\omega \hat{T}_{ab}} \int_0^\infty du\, e^{-u} \int_0^\infty e^{-i\omega u \hat{T}_a} p(\hat{T}_a) d\hat{T}_a \frac{d\omega}{2\pi} \\
&= \int_0^\infty \int_0^\infty du\, e^{-u} \frac{1}{2\pi} \int_{-\infty}^\infty e^{-i\omega(u\hat{T}_a - \hat{T}_{ab})} d\omega\, p(\hat{T}_a) d\hat{T}_a
\end{aligned}
\tag{A.21}
$$

Using the definition of dirac delta function:

$$
\begin{aligned}
p(\hat{T}_{ab}) &= \int_0^\infty \int_0^\infty du\, e^{-u} \delta(\hat{T}_{ab} - u\hat{T}_a) p(\hat{T}_a) d\hat{T}_a \\
&= \int_0^\infty \frac{1}{\hat{T}_a} e^{-\hat{T}_{ab}/\hat{T}_a} p(\hat{T}_a) d\hat{T}_a
\end{aligned}
\tag{A.22}
$$

This completes the derivation of (2.9).

B. DERIVATION OF THE TRANSMISSION COEFFICIENT FOR A NEGATIVE REFRACTIVE INDEX SLAB BETWEEN TWO DIFFERENT MEDIA

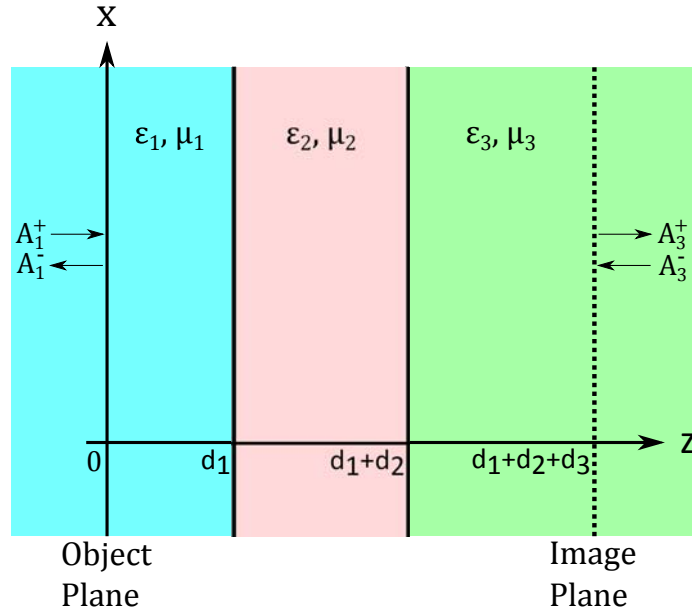This appendix is mainly dedicated to provide a detailed derivation of (5.1).

Fig. B.1. The geometry consists of a slab of thickness d_2 placed between two different media. The distance between the object plane and the left boundary of the slab is d_1, and the distance between the image plane and the right boundary of the slab is d_3.

The slab problem can be solved by the transverse transmission matrix theory [86]. Let us denote the amplitudes of positive and negative traveling waves at the object and image planes by $A_{1,3}^{\pm}$. These quantities can be related by the following equation

$$
\begin{bmatrix} A_1^+ \\ A_1^- \end{bmatrix} = M \begin{bmatrix} A_3^+ \\ A_3^- \end{bmatrix},
\tag{B.1}
$$

where the transverse transmission matrix, M, is

$$M = \begin{bmatrix} e^{jk_{z1}d_1} & 0 \\ 0 & e^{-jk_{z1}d_1} \end{bmatrix} \begin{bmatrix} \frac{Z_2+Z_1}{2Z_2} & \frac{Z_2-Z_1}{2Z_2} \\ \frac{Z_2-Z_1}{2Z_2} & \frac{Z_2+Z_1}{2Z_2} \end{bmatrix} \begin{bmatrix} e^{jk_{z2}d_2} & 0 \\ 0 & e^{-jk_{z2}d_2} \end{bmatrix} \begin{bmatrix} \frac{Z_3+Z_2}{2Z_3} & \frac{Z_3-Z_2}{2Z_3} \\ \frac{Z_3-Z_2}{2Z_3} & \frac{Z_3+Z_2}{2Z_3} \end{bmatrix} \begin{bmatrix} e^{jk_{z3}d_3} & 0 \\ 0 & e^{-jk_{z3}d_3} \end{bmatrix}.$$

$$(\text{B.2})$$

The first, third, and fifth elements in (B.2) are the wave transmission matrices for homogeneous media with thickness d_1, d_2, and d_3, respectively. Meanwhile, the second and fourth elements in (B.2) are wave transmission matrices for the two planar discontinuity interfaces in the structure, which can be derived from the continuity condition of transverse EM fields at the boundary.

Now we express the elements in M in terms of the reflection coefficients of two half spaces. The reflection coefficients from medium 2 back to medium 1 is

$$r_{12} = \frac{Z_2 - Z_1}{Z_2 + Z_1}, \tag{B.3}$$

and similarly the reflection coefficients from medium 3 back to medium 2 is

$$r_{23} = \frac{Z_3 - Z_2}{Z_3 + Z_2}. \tag{B.4}$$

Expressing the impedances in terms of r_{12} and r_{23} in (B.2) and carrying out the multiplication give

$$M = \frac{1}{(1+r_{12})(1+r_{23})} \begin{bmatrix} M_{11} & M_{12} \\ M_{21} & M_{22} \end{bmatrix}, \tag{B.5}$$

where the elements are

$$\begin{aligned}
M_{11} &= e^{j(k_{z1}d_1+k_{z2}d_2+k_{z3}d_3)} + r_{12}r_{23}e^{j(k_{z1}d_1-k_{z2}d_2+k_{z3}d_3)}, \\
M_{12} &= r_{23}e^{j(k_{z1}d_1+k_{z2}d_2-k_{z3}d_3)} + r_{12}e^{j(k_{z1}d_1-k_{z2}d_2-k_{z3}d_3)}, \\
M_{21} &= r_{12}e^{-j(k_{z1}d_1-k_{z2}d_2-k_{z3}d_3)} + r_{23}e^{-j(k_{z1}d_1+k_{z2}d_2-k_{z3}d_3)}, \\
M_{22} &= r_{12}r_{23}e^{-j(k_{z1}d_1-k_{z2}d_2+k_{z3}d_3)} + e^{-j(k_{z1}d_1+k_{z2}d_2+k_{z3}d_3)}.
\end{aligned} \tag{B.6}$$

To obtain the transmission and reflection coefficients of the slab with object and image planes specified in Fig. B.1, substitute $A_1^+ = 1$, $A_1^- = \Gamma$, $A_3^+ = T$, and $A_3^- = 0$ in (B.1), we obtain

$$T = \frac{(1+r_{12})(1+r_{23})e^{-j(k_{z1}d_1+k_{z2}d_2+k_{z3}d_3)}}{1 + r_{12}r_{23}e^{-j2k_{z2}d_2}}, \tag{B.7}$$

$$\Gamma = \frac{r_{12} + r_{23}e^{-j2k_{z2}d_2}}{1 + r_{12}r_{23}e^{-j2k_{z2}d_2}}e^{-j2k_{z1}d_1}. \tag{B.8}$$

A special case arises when medium 1 and 3 are the same so that $r \equiv r_{12} = -r_{23}$. Then the transmission and reflection coefficients can be expressed as

$$T = \frac{1 - r^2}{1 - r^2e^{-j2k_{z2}d_2}}e^{-j(k_{z1}d_1 + k_{z2}d_2 + k_{z3}d_3)}, \tag{B.9}$$

$$\Gamma = \frac{1 - e^{-j2k_{z2}d_2}}{1 - r^2e^{-j2k_{z2}d_2}}re^{-j2k_{z1}d_1}. \tag{B.10}$$

VITA

VITA

Yulu Chen was born in Yangzhou, China. He received his Bachelor's degree with first class honors in Electronic and Communications Engineering from the University of Hong Kong in 2010. In the same year he commenced his graduate studies at Purdue University. His research interests involve theoretical and numerical study of wave statistics in random media, as well as super resolution related problems. He graduated with a Ph.D. in Electrical Engineering in May 2015.